Chemical Science

Accepted Manuscript

Chemical Science

rsc.li/chemical-science

Volume 9
Number 1
7 January 2018
Pages 1-268

ISSN 2041-6539

ROYAL SOCIETY OF CHEMISTRY

EDGE ARTICLE
Xinjing Tang et al.
Caged circular siRNAs for photomodulation of gene
expression in cells and mice

This is an Accepted Manuscript, which has been through the Royal Society of Chemistry peer review process and has been accepted for publication.

Accepted Manuscripts are published online shortly after acceptance, before technical editing, formatting and proof reading. Using this free service, authors can make their results available to the community, in citable form, before we publish the edited article. We will replace this Accepted Manuscript with the edited and formatted Advance Article as soon as it is available.

You can find more information about Accepted Manuscripts in the Information for Authors.

ROYAL SOCIETY OF CHEMISTRY

rsc.li/chemical-science

ARTICLE

Two-Dimensional Conjugated Metal–Organic Frameworks for Electrochemical Energy Conversion and Storage

Xiao Li,[a] Xi Su,[b] Tan Su,[*b] Long Chen,[*b] Zhongmin Su[*ab]

Effective electrocatalysts and electrodes are the core components of energy conversion and storage systems for sustainable carbon and nitrogen cycles to achieve a carbon-neutral economy. Two-dimensional conjugated metal-organic frameworks (2D *c*-MOFs) have emerged as multifunctional materials for electrochemical applications benefiting from their similarity to graphene with remarkable conductivity, abundant active sites, devisable components, and well-defined crystalline structures. In this review, the structural design strategies to establish active components with a maximum degree through redox-active ligand assembly in 2D *c*-MOFs is briefly summarized. Next, recent representative examples of 2D *c*-MOFs applied in electrocatalysis (hydrogen/oxygen evolution and oxygen/carbon dioxide/nitrogen reduction) and energy storage systems (supercapacitors and batteries) are introduced. The synergistic effect of multiple components in 2D *c*-MOFs is particularly emphasized for enhanced performance in electrochemical energy conversion and storage systems. Finally, an outlook and challenges are proposed for realizing more active components, elucidating the reaction mechanism involving the derived structures, and achieving low-cost economy in practical applications.

1. Introduction

With the ever-increasing energy consumption and concomitant serious environmental problems associated with fossil fuels, high value-added chemical production and energy storage relying on renewable electrochemical devices have become an overwhelming trend for carbon-neutral economies.[1-2] Owing to their advantages of eco-friendliness, simple manipulation, and flexible configuration, electrochemical energy conversion and storage systems led to advanced progress in recent decades, including water-splitting electrolyzers, CO_2/N_2-reduction electrolyzers, fuel cells, supercapacitors, metal-air batteries, and rechargeable batteries.[3-5] Electrocatalysts and electrode materials are the core components of electrochemical devices and should possess the intrinsic features of well-defined structures with abundant active sites, efficient charge/mass transfer routes, and long-term chemical and structural stability to ensure excellent availability.[6-7] To date, the practical applications of most electrochemical materials are limited by their unsatisfactory energy conversion efficiency resulting from their high energy barriers and sluggish reaction kinetics.[8-9]

Precious metal-based materials are the most efficient electrocatalysts and electrode materials, but their high cost, scarcity, and poor stability restrict their wide application in electrochemical devices.[10-12] There is urgent development for highly effective, low-cost materials with clear structure-property relationships to address the above challenges and stimulate the rational design and regulation of electrochemical devices.

Metal–organic frameworks (MOFs) represent a class of typical crystalline materials with highly ordered porosity assembly by coordination bonds between metal ions/clusters and ligands and have various applications in gas sensing and storage, photo/electrocatalysis, and batteries, among others.[13-15] Owing to their insulating properties, traditional 3D MOFs are commonly used as precursors in electrochemical energy systems through pyrolysis, in which the corresponding products of carbon or metal oxides inherit the merits of large surface areas and abundant active sites, resulting in improved electrochemical performance.[16] However, uncertain fine structures greatly impede the investigation of structure-property relationships.[17] Two-dimensional conjugated MOFs (2D *c*-MOFs) are typically constructed using π-conjugated ligands equipped with *ortho*-substituted functional groups and transition metal ions through a square-planar coordination configuration.[18] 2D *c*-MOFs have demonstrated prominent applications, such as electronics, gas sensing, catalysis, magnets, and batteries, etc.[19-23] Benefitting from the graphene-like structures, 2D *c*-MOFs exhibit two types of electron transfer pathways: strong in-plane conjugation and

[a.] School of Chemical and Environmental Engineering, Jilin Provincial Science and Technology Innovation Centre of Optical Materials and Chemistry, Jilin Provincial International Joint Research Center of Photo-functional Materials and Chemistry, Changchun University of Science and Technology, Changchun 130012 (China)..

[b.] State Key Laboratory of Supramolecular Structure and Materials, College of Chemistry, Jilin University, Changchun, 130012 (China).

ARTICLE

Journal Name
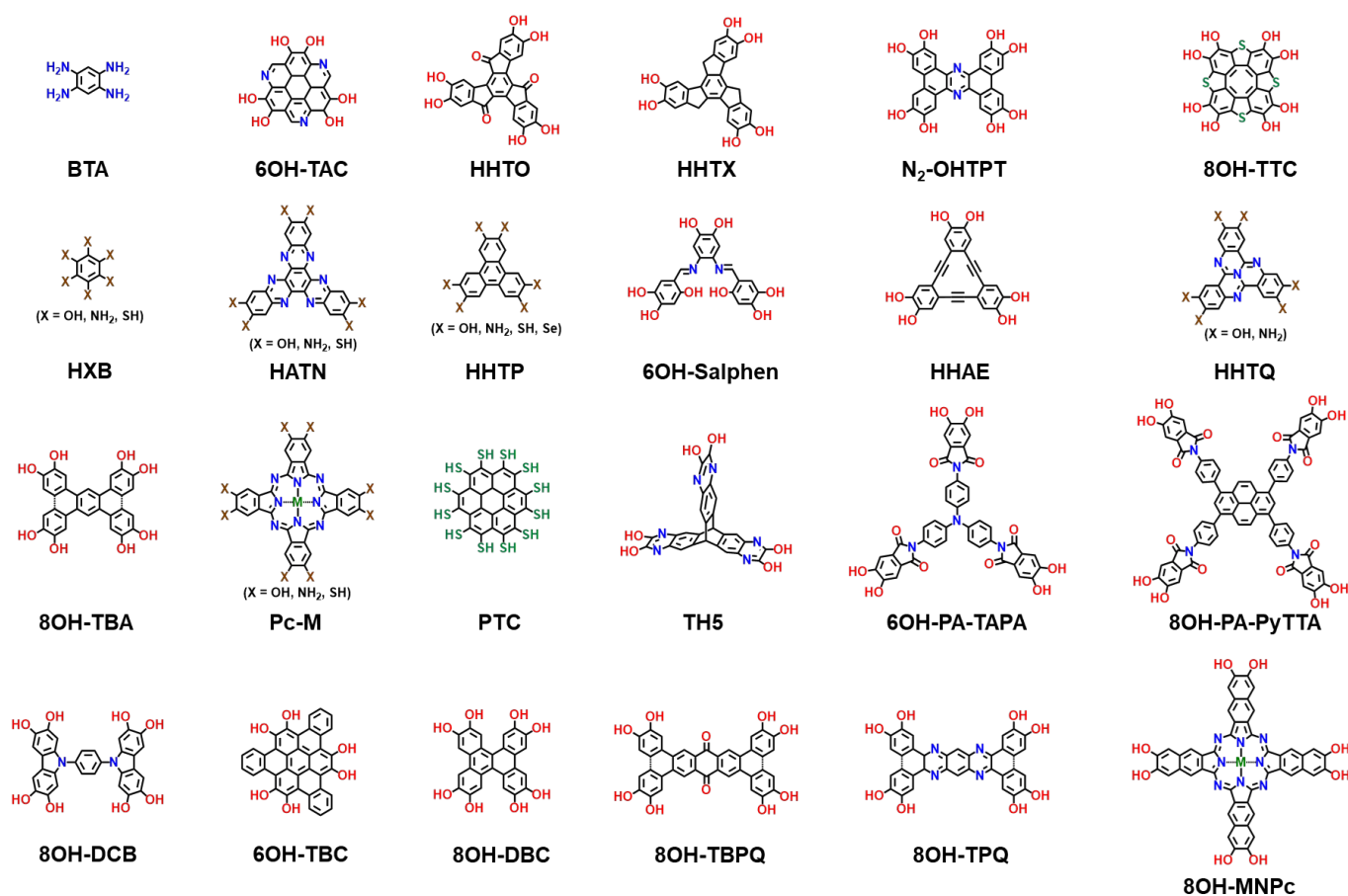
Chemical Science Accepted Manuscript

Fig. 1 Typical redox ligands reported for 2D *c*-MOFs.

weak interaction of out-of-plane π-π stacking, which cooperatively result in decent intrinsic electrical conductivities.[24] Moreover, together with the abundant and accessible active sites exposed in the planes and channels, effective mass transport, and device feasibility, 2D *c*-MOFs can be utilized as multifunctional materials for electrochemical energy storage and transformation via integration into electrolyzers and batteries.[25]

Currently, the investigation of 2D *c*-MOFs is mainly devoted to the synthesis of new types of structures based on molecular design, and the search for new unexploited applications. For electrochemical applications, 2D *c*-MOFs have been used only for a few decades. Challenges remain regarding insufficient performance and unambiguous structural-property correlations. Several recent excellent reviews on MOFs and carbon-rich conjugated frameworks have discussed ligand design, synthetic methods, conductive mechanisms for electrode materials, and electrocatalysts.[26-29] In this article, we highlight and sum up recent progress in 2D *c*-MOFs for applications in electrochemical energy conversion and storage systems, focusing on the synergistic effect of redox π-conjugated ligands and metal ions in charge transfer and mass transport processes. First, the design of redox ligands is introduced. Subsequently, representative 2D *c*-MOFs used in

electrocatalytic water splitting, oxygen/carbon/nitrogen reduction for energy conversion, supercapacitors, and metal-ion batteries for energy storage are introduced. This review offers insights into the synergistic effects of ligands and metal ions to establish the maximum number of active sites, thereby supporting the emerging improvement of 2D *c*-MOFs in electrochemical energy applications.

2. Ligand design strategies, active sites engineering, and tailor-made functions

Conjugated ligands with π-electron delocalization and redox properties are considered to be electrochemically active components that play vital roles in energy storage and conversion processes, including charge/mass transfer, key intermediate adsorption, product formation, and desorption.[30-32] The ligands used to construct 2D *c*-MOFs are usually equipped with *ortho*-substituted functional groups, such as -OH, -NH$_2$, -SH, and -SeH. Transition metal ions such as Co^{2+}, Cu^{2+}, Mn^{2+}, Sn^{2+} and Zn^{2+}, in 2D *c*-MOFs display square-planar coordinated modes through d-π conjugation, driving the growth on the second dimension for two-dimensional conjugated structures, always alongside 1D channels in the third dimension through π-π stacking interactions. Against the background of current

Journal Name ARTICLE

progress, designing and synthesizing more novel ligands cooperating with more redox-active sites, such as various unsaturated bonds and heteroatoms, is greatly significant in the development of the synthesis chemistry of 2D *c*-MOFs.

The topological structures and channel types of 2D *c*-MOFs can be predicted based on the symmetry of the organic ligands, which offers promising opportunities for designing frameworks with special functions. Typically, trigonal organic ligands based on benzene and polyacene aromatic cores of with C_3 or C_6 symmetry are inclined to form hexagonal lattices and channels.[33] Tetragonal and rhombic lattices are often constructed using tetrasubstituted organic ligands with D_2 symmetry containing porphyrin, phthalocyanine, and dibenzochrysen.[34] Kagome lattices are often obtained using ligands with D_{6h} symmetry, such as perthiolated coronene (PTC).[35] Two stacking modes are most common in 2D *c*-MOFs, including the A-A stacking (face-to-face) mode and the slipped parallel mode, both of which feature one-dimensional ordered open channels. To date, with the exception of the first 2D *c*-MOF of Co-HHTP with clear single-crystal structures,[36] most 2D *c*-MOFs are obtained in the form of polycrystalline powders, which cannot be tested by the single-crystal X-ray diffraction (SXRD) technique resulting from the rapid kinetics in the formation process and strong in-plane bonds of metal and heteroatoms.[37] Considering the difficulty of controlling the coordination rate of metal ions and planar ligands, nonplanar organic linkers are promising candidates to synthesize planar 2D *c*-MOFs, first proposed by our group in 2020.[34] A series of nonplanar ligands with various cores has been employed to construct planar 2D *c*-MOFs with high conductivity and enhanced crystallinity.[38] The good solubility of nonplanar ligands ensures the easy synthesis and purification of high-quality single crystals. Flexible and decoratable structures can fulfill unprecedented topologies and custom-made functions through rational design and synthetic methods. For example, Cu-DCB-MOFs are synthesized utilizing a versatile "Rotor-Stator" strategy with highly crystalline structures, endowing the exceptional high performance for zinc-ion hybrid supercapacitors.[39]

Multiple types of redox activities influenced by the metal ions and ligands in 2D *c*-MOFs play crucial roles in charge/mass transfer and metal ion storage for electrochemical energy conversion and storage applications. The square planar coordinated MX_4 (M = Cu^{2+}, Ni^{2+}, Co^{2+}, X = N, O, S, Se) is noted for its multiple chemical states and variations in electrochemistry, which can coexist in the same frameworks, such as Cu^{2+}/Cu^+ in Cu(HTQ).[31] In contrast, unsaturated bonds, such as C=O and C=N, exhibit redox activity via single/double-bond conversion. Recent representative examples of the redox ligands are summarized in Fig. 1. For example, HHTP in Zn-HHTP exhibits reversible oxidation and reduction through the C=O to C-O· radical or C-O bond of semiquinone, which is responsible for the successive PF_6^- and Li^+ storage in sodium-ion batteries.[37]

The unsaturated C=O bonds also endow HHTQ-based 2D *c*-MOFs with multifunctional applications in CO_2RR, NO_2 sensing, and lithium-ion batteries.[41-43] For $Zn_3(HHTQ)_2$, a redox synergy strategy involving transition metal ions and ligands was used to balance the reactivity for NO_2 sensing with remarkable cycling stability. Unsaturated C=N bonds were confirmed to be the predominant active sites through coordination or redox interactions in the form of -N^+- and conductivity variations. $Cu_3(HHTQ)_2$ displays excellent performance to reduce CO_2 to methanol, with a low overpotential for high Faradic efficiency. The nitrogen-rich core of tircycloquinazadine (TQ) facilitates the capture of CO_2 with a Gibbs free energy ΔG of -0.24 eV, showing good CO_2 adsorption ability.[42] For lithium storage, TQ was verified as redox active component reacted with Li^+ for the first time, synergistically working with CuO_4 in Cu-HHTQ, resulting in ultrahigh capacity and superior cyclability for lithium-ion batteries.[43] In general, ligands with redox activity can establish the largest utilization degree of multicomponent 2D *c*-MOFs by synergistic effects, further helping to elucidate the structure-property relationships at the molecular and atomic levels, which can be beneficial for promising electrochemical materials through rational design and skillful synthesis of 2D *c*-MOFs.

3. Applications in electrochemical energy conversion systems

In the field of electrochemical energy conversion, there are several main reactions, including hydrogen evolution reaction (HER), oxygen evolution reaction (OER), oxygen reduction reaction (ORR), carbon dioxide reduction reaction (CO_2RR), and nitrogen reduction reaction (NRR). The HER and OER can be integrated into a water electrolyzer for water splitting, and the OER and ORR can be combined for Zinc-air batteries.[44-45] For electrocatalytic reactions, the sluggish kinetics, high activation energy barriers, and large overpotentials heavily hinder the practical application of transitional-metal-based electrocatalysts. Developing highly efficient non-precious metal electrocatalytic materials with clear structural-activity relationships is a major challenge.

2D *c*-MOFs exhibit well-designed crystal structures and single-atom-like catalyst behavior, which can act as an ideal model for fundamental mechanistic investigations of structure-performance relationships at the atomic level.[45] The conjugated planar structures contribute to intrinsic electrical conductivity, abundant active sites, and clear pathways for electron and mass transfer, positioning 2D *c*-MOFs as promising electrocatalysts. Furthermore, the flexible variation of components with ligands induces specific topologies that can effectively modulate the electronic structures of active sites, which is crucial for enhancing electrocatalytic performance.[46-47] The effect of ligands on 2D *c*-MOFs has attracted increasing research attention.
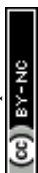
ARTICLE

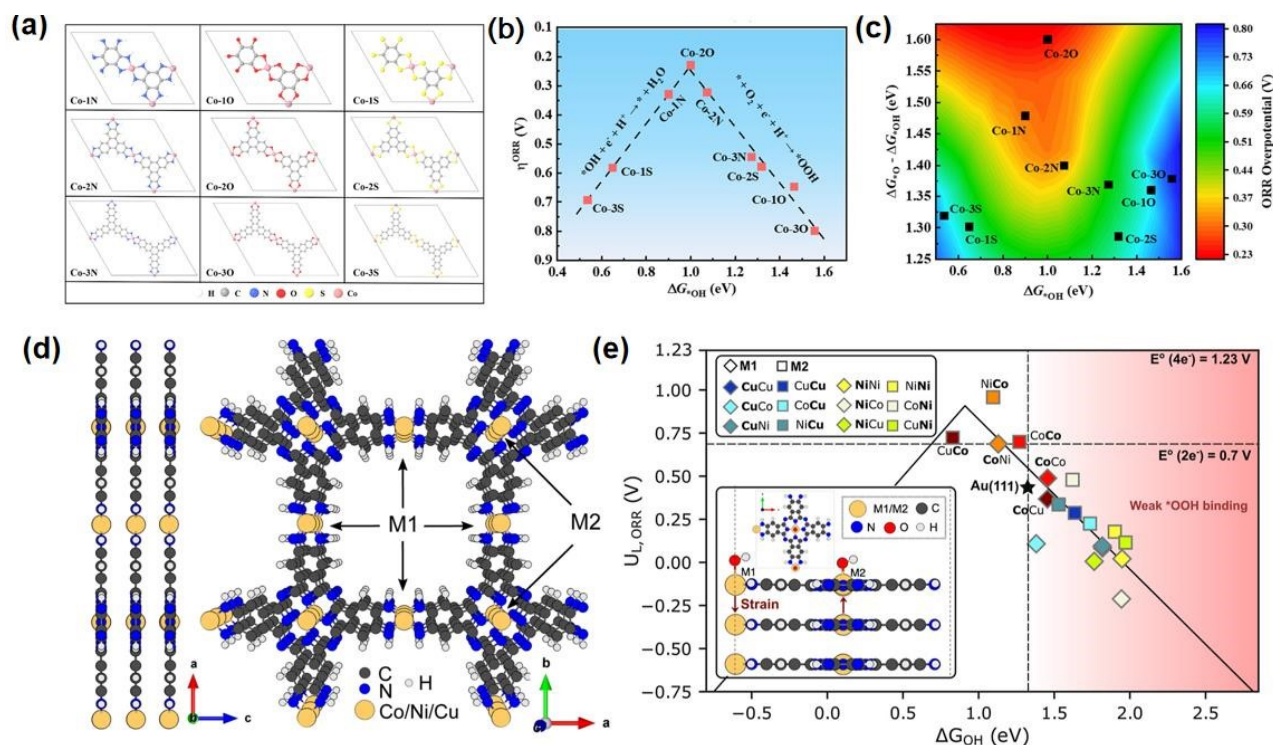**Fig. 2** (a) Scheme of different organic ligands in 2D Co-MOFs. (b-c) Volcano plots of DG*OH versus overpotentials. (d) MOF structural model from side and top view. (e) Volcano plot of MOFs (each site) toward four-electron ORR for flat layers. (a)-(c) were reproduced with permission from ref 54. Copyright 2023 American Chemical Society. (d)-(e) were reproduced with permission from ref 55. Copyright 2024 American Chemical Society.

Electrocatalytic activity is determined by electron delocalization and conductivity, both of which are tightly corresponded to the architecture of the ligands. Furthermore, the functional groups in the organic ligands usually act as synergistic catalytic sites.

3.1 ORR electrocatalysts

ORR is a crucial half-reaction of fuel batteries and metal-air batteries. M-N-C are the most considered catalytically active sites for ORR. Since 2016, $Ni_3(HTTP)_2$ has been applied in ORR for the first time, showing that the NiN_4 units act as active sites.[48] Following $PcCuO_8$-Co on carbon nanotubes (CNT) in 2019, CuO_4 motifs were confirmed as ORR active sites owing to the favorable optimization of the electronic structure, resulting in moderate interaction with the key intermediates of *OOH.[49] Furthermore, the in-plane sites of conjugated ligands have also been proposed as ORR active sites originating from their large limiting potential and strong oxygen binding.[50-52] In 2023, a di-copper-based 2D c-MOF of CuPc-CuO_4 films combined with a Ni-nitrilotiacetic acid (Ni-NTA)-functionalized graphene electrode was investigated for the ORR using electrochemical resonance Raman spectroscopy.[53] The reduction transitions of $Cu^{II} \rightarrow Cu^{I}$

and $CuPc_x$ increased π-conjugation, enabling catalysis. The Cu^{II}/Cu^{I} states of CuO_4 and CuPc are the active sites for ORR.

Coordination atoms can adjust the electronic structures of the metal sites. In Fig. 2a, Dai and colleagues used density functional theory (DFT) to investigate the regulation effect of diverse organic ligands on the ORR activity in 2D c-MOFs.[54] Co-2O based on HHTP displays superior ORR activity via 4e- reduction route with relatively low overpotential of 0.23 V (Fig. 2b and 2c). The Co sites in Co-2O possess a high-spin state, regulated by the synergistic effect of triphenylene and hydroxyl groups, which promotes interaction with the key intermediates of *OH for enhanced ORR performance. Moreover, all Co-MOFs displayed excellent electrochemical and thermodynamic stabilities. Jaramillo et al. introduced dual MN_4 (M = Co, Ni, Cu) sites in a 2D phthalocyanine MOF as ORR electrocatalysts, in which one metal ion as M2 coordinates with an amine node and the other metal ion is bonded to the phthalocyanine center (M1) (Fig. 2d).[55] The Co sites dominate the catalytic activity and control the layer distance. The low degree of saturated M-N bonds at the M2 sites promotes the strong adsorption of OH, displaying more dominance in catalytic activity, while the M1 sites greatly influence the selectivity. In Fig. 2e, the bimetallic
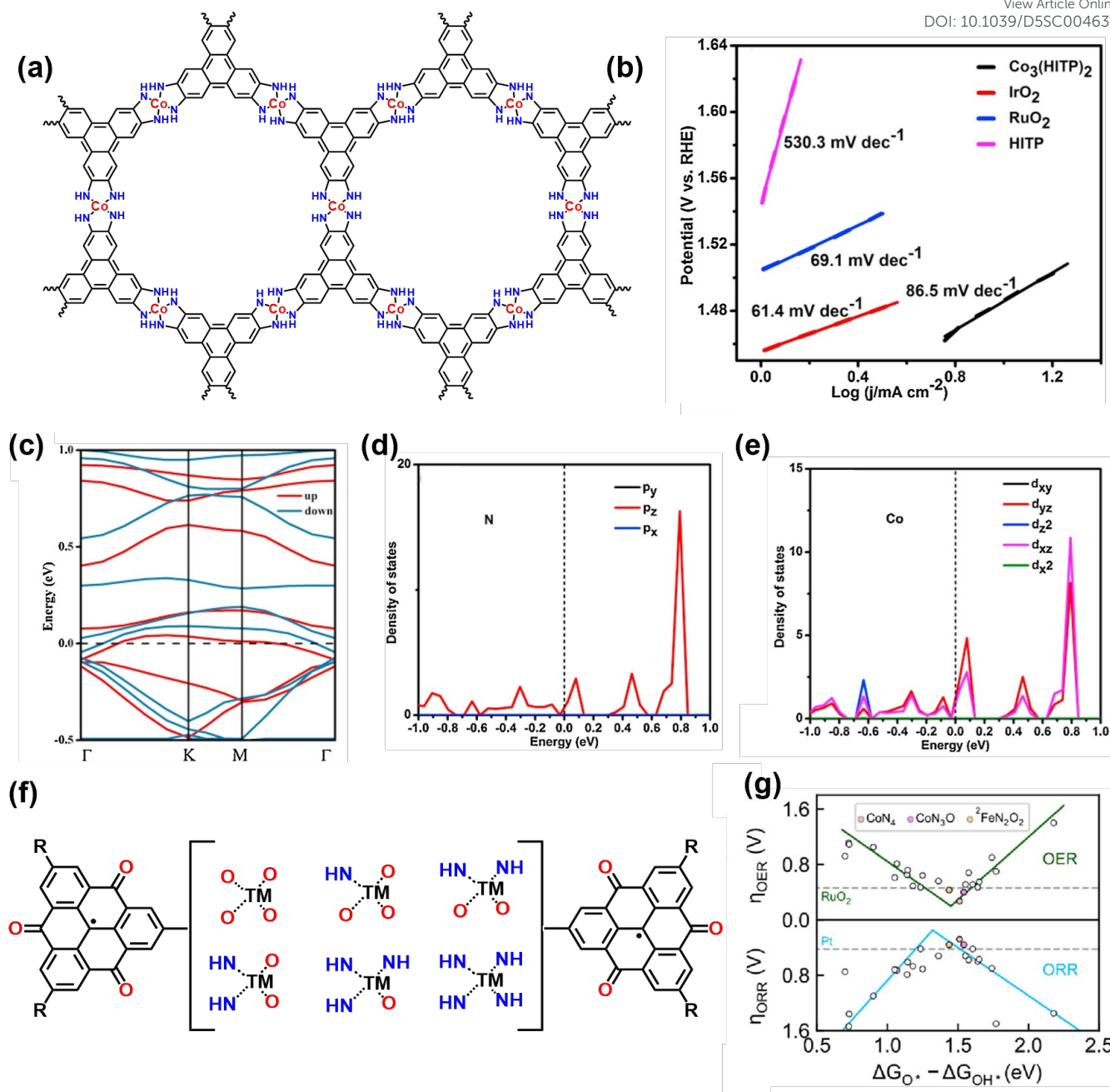
Fig. 3 (a) The structure of $Co_3(HITP)_2$. (b) LSV curves of $Co_3(HITP)_2$ and controlled samples. (c-e) total and partial DOS of $Co_3(HITP)_2$. (f) Structure schematics of TMN_xO_{4-x}-TOT systems. (g) 2D volcano plot of Gibbs free energy difference between *O and *OH (DGO*−DGOH*) versus the η_{OER} and η_{ORR}. (a)-(e) were reproduced with permission from ref 57. Copyright 2020 Elsevier. (f)-(g) were adapted with permission from ref 61. Copyright 2023 American Chemical Society.

combination of Ni-Co is predicted to obtain the highest ORR activity with 0.27 V as the minimum overpotential based on the optimized OOH*-OH* value. This work highlights the tailored function of electrocatalysis by tuning the strain of the metal sites and coordination environments.

3.2 OER electrocatalysts

The OER is a key half reaction in electrocatalytic water splitting and metal-air batteries. The four-electron transfer process results in slow kinetics and high activation energy barriers of

OER; thus, effective and low-cost electrocatalysts are urgently needed. The CoN_4 sites were verified to be efficient OER-active sites. The large d-π conjugation required for a fast electron transfer capability makes 2D *c*-MOFs highly promising OER electrocatalysts.

As one of the smallest conjugated ligands, hexaaminobenzene (HAB) possesses dense redox-active sites that enable charge transfer between metal nodes and the plane of the ligand. The ultrathin 2D nanosheets of Co-HAB-NSs with a thickness about 4.5 nm, displayed a low overpotential of 310

ARTICLE

mV at 10 mA·cm^{-2} in KOH with good durability.[56] The nitrogen richness of HAB endows Co-HAB-NSs with highly dense active sites for electrocatalysis. Through DFT calculations, the overpotentials of the carbon atoms from the benzene rings were lower than those of the Co sites, implying a higher catalytic activity. This work indicates that dense active sites from redox ligands can greatly improve the catalytic performance through strong π-d conjugation with 1D channels to accelerate charge transfer.

The larger conjugated ligands of HITP compared to the HAB-constructed 2D *c*-MOF of Co$_3$(HITP)$_2$ (Fig. 3a) presented a higher electrical conductivity of 1150 S·m^{-1} than that of graphene.[57] Co$_3$(HITP)$_2$ displayed a remarkable OER performance with an overpotential of 254 mV to reach 10 mA·cm^{-2} (Fig. 3b). Both the calculated density of states (DOS) and electronic band structure of Co$_3$(HITP)$_2$ are metallic, resulting from the p-d conjugation of p$_z$ orbitals from N atoms and the d$_{yz}$ and d$_{xz}$ orbitals from Co (Fig. 3c-3e). The high content (23.44 wt%) of the active sites of the CoN$_4$ sites ensured excellent OER performance. The structures flexibility through ligands controlled of 2D *c*-MOFs offers more opportunities for the OER through electronic structure modulation.

Co-HHTP also show OER activity with overpotential of 245 mV at 10 mA·cm^{-2}, exceeding most reported Co-MOFs.[58] DFT calculations demonstrated the moderate d-band centers and favorable electrical conductivity of Co-HHTP, promoting the adsorption/desorption capability of oxygen-containing intermediates. *In situ* Raman spectroscopy confirmed the formation of CoOOH as the real active sites in the OER process.

Bifunctional OER/ORR catalysts based on 2D *c*-MOFs, such as Ni$_x$Co$_{3-x}$(HITP)$_2$[59] and (Mn/Fe)$_3$(HIB)$_2$,[60] have been developed as bimetallic frameworks. Jing et al. propose a simple descriptor as "spin momentum" of the metal center as the universal principle to assess the OER/ORR activity by machine learning activity (Fig. 3f).[61] 2D conjugated organic linkers provide different coordination environments as the core and functional groups work together. The hybridization of d-p interactions involves *p* orbitals from the O/N/C of ligands and d orbitals from metal ions, which redistribute the electronic states of the metal centers. Taking TMN$_x$O$_{4-x}$-TOTs as models, CoN$_4$-TOT exhibits bifunctional OER/ORR activity with η$_{OER}$=0.28 V and η$_{ORR}$=0.26 V in Fig.3g. This work can guide the screening of 2D *c*-MOFs with various organic ligands and reveal the intrinsic correlation between coordination properties and catalytic performance.

The conjugation of ligands can largely decide electrocatalytic process by enhancing charge-transfer kinetics. Using DFT calculations, Dai et al. reported a sequence of 2D *c*-MOFs (TM-HHTC) for the OER/ORR performance investigation.[62] Co-HHTC exhibited superior OER/ORR activity with an overpotentials of 0.21 V. Co metal sites and Co-O bonds show suitable d-band center values and medium charge accumulation, which are key factors for the OER/ORR activity. Moreover, the interaction between the 2s orbital of oxygen and the 4p$_z$ orbital of Co can regulate catalytic activity.
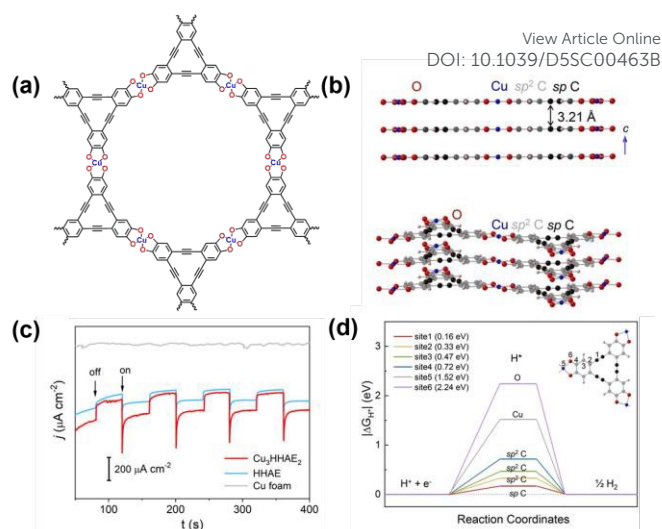
3.3 HER electrocatalysts

Fig. 4 (a) The structure of Cu$_3$HHAE$_2$. (b) Views parallel to the ab plane. (c) Photocurrent-time plots for Cu$_3$HHAE$_2$ and HHAE cathodes at 0 V vs. RHE. On: illumination on; off: illumination off. (d) Free-energy diagram for H$_2$- evolution via a single-site reaction pathway: 1, 2, 3, 4, 5, 6 denote different active sites of Cu$_3$HHAE$_2$. Reproduced with permission from ref 65. Copyright 2022 Wiley.

Electrocatalytic water splitting is considered as the most efficient and simple method for hydrogen production. In 2D *c*-MOFs, Co-S bonds are usually recognized as active sites for the HER, such as Co$_3$(BHT)$_2$ and Co$_3$(HTTP)$_2$.[63] Unsaturated NiN$_2$ sites also play a decisive role in the HER.[64] Sarkar reported TMPc-Cu-O MOFs for water splitting, in which TM = Fe, Co, and Ni were coordinated with the core of Pc and Cu in the skeleton. CoPc-Cu-O displays smallest overpotentials of 0.11/0.65 V for HER/OER, in which the C atoms from Pc units and Cu sites are confirmed as the active sites for HER and OER, respectively.

Cu$_3$HHAE$_2$ comprises CuO$_4$ units and *sp*-carbons from the C≡C bond arylene-ethynylene macrocycle ligand (Fig. 4a-4b).[65] Incorporated with the deficient electron properties of acetylene units, the acidity of the functional group (-OH) increases, resulting in reversibility of the metal-ligand bonds. As shown in Fig. 4c, Cu$_3$HHAE$_2$ was used as a photoelectrode for hydrogen generation, as uthe first case of 2D *c*-MOFs, achieving approximately 260 μA·cm^{-2} at 0 V versus a reversible hydrogen electrode (RHE). The C≡C bonds with low ΔG$_{H*}$ value of 0.17 eV are served as active sites for HER (Fig. 4d).

3.4 CO$_2$RR electrocatalysts

The CO$_2$ reduction reaction usually proceeds via various reaction routes with electron numbers ranging from 2 to 18, harvesting various products such as CO, CH$_3$OH, HCOOH, CH$_4$, C$_2$H$_5$OH, C$_2$H$_4$ and so on.[66] The selectivity of the CO$_2$RR depends on the type of metal ion, in which high-value-added carbon products are often generated by Cu species. CO$_2$RR involves three main steps: (1) CO$_2$ molecules are adsorbed and activated on catalytic sites; (2) proton migration and electron transfer induce C-O bonds broken and C-H bonds formed; and (3) release of the corresponding products and diffusion into the electrolyte.

Successive and complex reaction steps result in huge challenges, such as high energy barriers, slow reaction kinetics, difficult separation of raw materials and products, and inferior selectivity and stability. 2D *c*-MOFs with planar structures with highly dense and exposed active sites and tailored structures can solve the above challenges by integrating multiple active components from redox ligands or dual metal sites.

Fig. 5 (a) Synthesis of $M_3(HHTQ)_2$ (M=Cu, Ni), (b) LSV curves for $Cu_3(HHTQ)_2$ in Ar (grey line) or CO_2 (orange line) saturated 0.1 M $KHCO_3$ electrolyte with a scan rate of 5 mVs^{-1}. (c) CH_3OH FEs at different potentials. (d) The selectivity for each product (CH_3OH and H_2). (e) Free-energy profiles of CO_2 on MO_4 units. (f) Synthetic process of HATNA-Cu-MOF. (g) LSV curves of HATNA-Cu-MOF in Ar- and CO_2-saturated 0.1 M $KHCO_3$ electrolytes. (h) Potential dependent Faradaic efficiencies of different reduction products. (i) Chronoamperometry and $FE(CH_4)$ of HATNA-Cu-MOF at 1.5 V. (j) Comparison of CH_4 Faradaic efficiencies between HATNA-Cu-MOF, HATNA-6OH and the model compound. (a)-(e) were adapted with permission from ref 42. Copyright 2021 Wiley. (f)-(j) were reproduced with permission from ref. 68. Copyright 2021 Wiley.

Feng and coworkers designed a bimetallic 2D *c*-MOF of PcCu-O_8-Zn as an effective electrocatalyst through CO_2RR to produce CO.[67] The selectivity of CO was 88% with a turnover frequency (TOF) number of 0.39 s^{-1} and long-time stability (>10 h). Moreover, syngas can be modulated from 1:7 to 1:4 H_2/CO by changing working potentials and the metal centers. *Operado* spectroelectrochemistry and DFT calculations indicated the synergistic catalytic mechanism of the two metal units, in which ZnO_4 can act as the catalytic site for the CO_2RR, while CuN_4 promotes the adsorption and protonation of CO_2. Ligands with various heteroatoms and cores make decisive roles in the CO_2RR.

The coordination environment of the metal nodes can also participate in the catalytic process of the CO_2RR.

2D *c*-MOFs based on benzene cores can exhibit excellent electrical conductivity and highly dense metal sites, which are attractive for the CO_2RR. The rationally modified ligands can be investigated as an efficient method to improve the CO_2RR of the objective products. In 2021, our group used a nitrogen-rich tricycloquinazoline (TQ)-based catechol ligand (HHTQ) to construct 2D *c*-MOFs: $M_3(HHTQ)_2$ (M = Cu, Ni) under solvothermal conditions (Fig. 5a).[42] Alongside the graphene-like porous sheets and single-atom catalyst characteristics, $Cu_3(HHTQ)_2$ exhibited excellent CO_2RR activity, in which the Faradic efficiency (FE) of the CH_3OH product reached 53.6% at a low overpotential of 0.4 V (Fig. 5b-5d). The introduction of the TQ moiety helped capture and catalyze CO_2 synergistically with CuO_4 for the CO_2RR (Fig. 5e). Wang et al. reported a nitrogen-rich ligand-based 2D *c*-MOF (HATNA-Cu-MOF), as shown in Fig. 5f.[68] The exposed N sites displayed high affinity for CO_2. As shown in Fig. 5g-5j, the HATNA-Cu-MOF exhibited excellent performance for the conversion of CO_2 to CH_4. The FE of CH_4 was 78% at 8.2 $mA·cm^{-2}$ with good durability for 12 h at -1.5 V.

Heterodimetal Sn···Cu dual sites were integrated into CuSn-HAB to improve asymmetric C-C coupling in the CO_2RR.[69] CuSn-HAB depicts superior CO_2 conversion activity for ethanol production, which shows FE of 56(2)% with at 68 $mA·cm^{-2}$ at -0.57 V (vs RHE), and no significant degradation of current density operated for continuous 35 h. The SnN_2O_2 units showed enhanced affinity for oxygen, which facilitated the production of the key intermediate $*OCH_2$. Compared with Cu···Cu sites, which tend to produce ethylene, Cu···Sn sites exhibit more thermodynamically favorable interactions between $*CO$ and $*OCH_2$ through asymmetric C-C coupling, yielding ethanol products.

3.5 NRR electrocatalysts

The NRR for converting N_2 to NH_3 in 2D *c*-MOFs is still rare and in its infancy. Because of the relative high energy (944 kJ/mol of N≡N bonds), N_2 activation is the most challenging step for the NRR. $Co_3(HTTP)_2$ nanoparticles show NH_3 produced rate of 22.14 μg h^{-1} mg^{-1} cat with FE of 3.4% at -0.4 V vs RHE.[70] Jing et al. employed DFT calculations to elucidate the influence of heteroatoms in MN_4 patterns on NRR activation.[71] $Mo_3(C_6S_6)_2$ demonstrated the best activity with minimal of 0.37 V, following by the pathway of enzymatic nitrogenase. Babarao and coworkers investigated the NRR activity of the MN_4 units in 2D porphyrin frameworks as single-atom catalysts (Fig. 6a).[72] DFT calculations indicated that the bonding state of the M-N bonds and the antibonding state of the N-N bonds are crucial and contribute equally to the N≡N bonds activation (Fig. 6b). As shown in Fig. 6c, Ti-TCPP MOF exhibited exclusive NRR selectivity with a potential of -0.35 V in aqueous solutions. In the final step of protonation, Ti-TCPP exhibits a low kinetic energy barrier (1.43 eV, Fig. 6d), making Ti-TCPP a promising candidate electrocatalyst for NRR. Xu et al. explored the 2D *c*-MOFs of $TM_3C_{18}N_6X_{12}$ as NRR electrocatalysts using DFT calculations.[73] Coordinated atoms significantly influence the NRR performance of the 2D *c*-MOF based electrocatalysts.
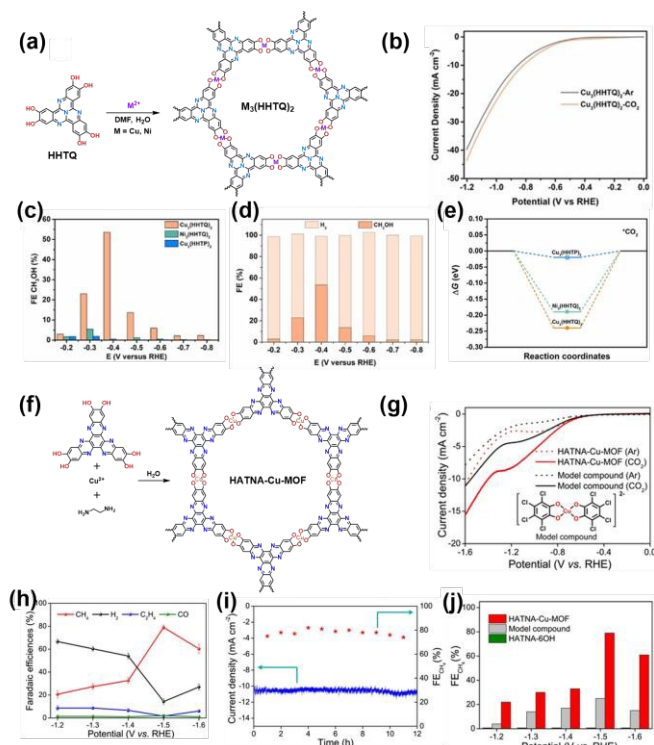
$Os_3C_{18}S_{12}N_6$ shows a lowest overpotential of 0.28 V through the distal pathway. The σ-acceptance-π* donation influences the adsorption and activation processes of N_2. Two descriptors were proposed to assess the catalytic activity during the N_2 adsorption process: the electronegativity of the metal atoms before and after the adsorption of N_2 ($\Delta Q_{TM}X_{TM}$), and the valence electron transfer product.

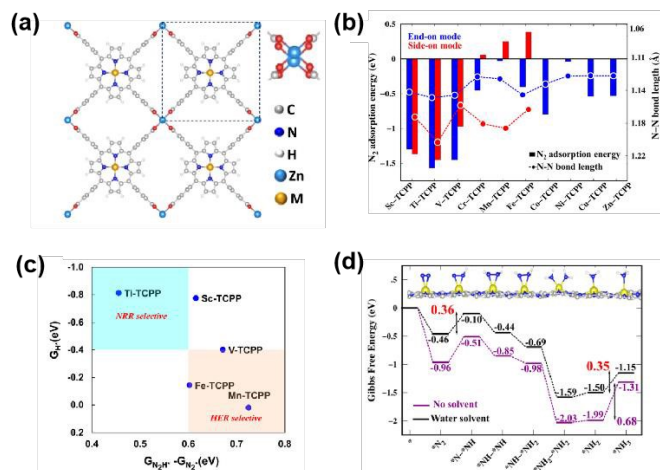**Fig. 6** (a) the optimized structure of M-TCPP 2D-MOFs with the paddlewheel $Zn_2(CO_2)_4$ linker. (b) N_2 adsorption energies and N-N bond lengths of N_2 adsorbed in perpendicular and parallel modes in M-TCPP MOFs. (c) NRR selectivity plots of the M-TCPP MOFs with lower limiting potentials. (d) Free energy diagram of enzymatic NRR on Ti-TCPP. Reproduced with permission from ref 72. Copyright 2024 American Chemical Society.

4. Applications in electrochemical energy storage systems

Electrochemical energy storage systems mainly include supercapacitors and metal-ion batteries, which play significant roles in our daily lives and human society, and have roused wide attention in the past few decades. Supercapacitors rely on charge storage via a surface-controlled process, delivering a ultralong cycle life, high power density, and free maintenance, but a low energy density. Metal-ion batteries with Faradaic redox reactions by bulk diffusion-controlled processes generally focus on higher rate performance and energy density with long-term cycle stability and safety. Electrode materials play decisive roles in both supercapacitors and metal-ion batteries, and can directly determine their performance. Large conductivity and high redox activity are two common features of highly active electrode materials. The higher conductivity can induce the faster charge transfer among active sites and substrates, which is benefit for energy storage process in supercapacitors and metal-ion batteries. For this purpose, 2D c-MOFs with high intrinsic electrical conductivity (up to 2500 S·cm⁻¹)[74] and tunable redox sites (metal nodes and redox ligands) are integrated into the frameworks to facilitate fast electron transport and reversible migration of metal ions. Moreover, the regular channels and large surface area of 2D c-MOFs can provide clear pathways and space for ion transport and storage. 2D c-MOFs

have aroused growing research interest in electrochemical energy storage fields and have shown excellent rate capability and splendid activity.

4.1 Supercapacitors

The active materials in supercapacitors depend on different charge-storage capacitances, including physical ion adsorbents that induce electrical double-layer (EDL) capacitor materials and surface Faradaic redox reactions, resulting in pseudocapacitor materials. In 2D c-MOFs, both metal nodes and redox organic linkers can exhibit capacity, often with different charge storage mechanisms, of which the synergistic contribution produces unprecedented supercapacitor performance.
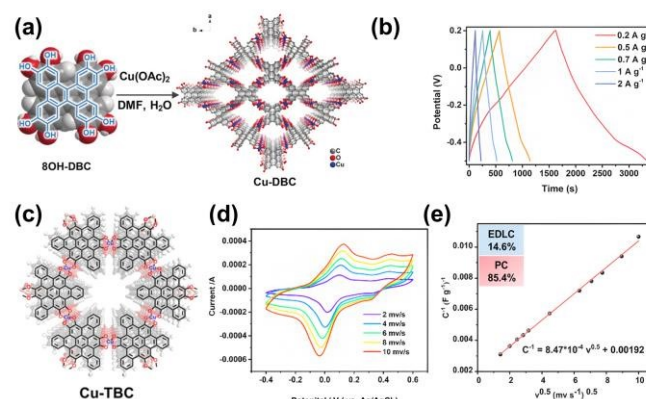

Fig. 7 (a) Synthesis of Cu-DBC. (b) GCD profiles collected at different current densities. (c) Structure of Cu-TBC. (d) CV curves of Cu-TBC at different scan rates. (e) Trasatti plot of the reciprocal of the gravimetric capacitance (C g⁻¹) against the square root of the scan rate. (a)-(b) were reproduced with permission from ref 34. Copyright 2020 Wiley. (c)-(e) were reproduced with permission from ref 77. Copyright 2023 Royal Society of Chemistry.

In 2017, Ni_3HITP_2 with high conductivity of exceeding 5000 S·m⁻¹,[75] as the first case of 2D c-MOFs, exhibits gravimetric capacitance of 111 F·g⁻¹ and areal capacitance of 18 μF·cm⁻² at 0.05 A·g⁻¹, predominately by double-layer capacitance mechanism. In 2018, Bao and colleagues reported Cu/Ni-HAB 2D c-MOFs with redox activity as submillimeter-thick electrochemical supercapacitors.[76] Bulk Ni-HAB and Cu-HAB showed large capacitances of 420 and 215 F·g⁻¹, respectively, in which HAB reversible redox reactions contributed to the primary pseudocapacitors.

In 2020, we reported redox ligand DBC-based conjugated MOFs of Cu-DBC under solvothermal conditions, which showed a high electrical conductivity ($\approx$ 1.0 S·m⁻¹) with typical semiconducting behavior (Fig.7a).[34] The charge storage mechanism of supercapacitors for Cu-DBC exhibited both pseudocapacitance and double-layer capacitance owing to the synergistic effect of the DBC ligands and copper bis(dihydroxy) nodes, resulting in a gravimetric capacitance of 479 F·g⁻¹, a large areal capacitance of 879 mF·cm⁻², and a volumetric capacitance of 22 F·cm⁻³ (Fig. 7b). Recently, we synthesized a 2D c-MOF of Cu-TBC using a hexahydroxytribenzocoronene ligand (6OH-TBC) as the electrode material for supercapacitors (Fig.7c).[77] Large

conjugated aromatic ligands can enhance the conductivity and stability of 2D *c*-MOFs. Featuring decent electrical conductivity of ~0.068 S·m^{-1}, Cu-TBC shows dominant capacitance in -0.4 V~ 0.6 V (vs Ag/AgCl) with gravimetric capacitance of 474.8 F·g^{-1} at 0.2 A·g^{-1} (Fig. 7d) in 0.1 M H$_2$SO$_4$.In Fig. 7e, the charge storage mechanisms were also influenced by the electric double layer and pseudocapacitance.
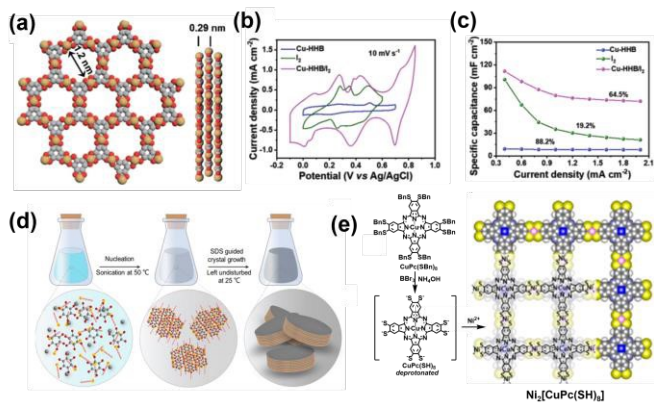

Fig. 8 (a) The unit-cell structures of Cu-HHB derived using AB slipped-parallel stacking models. (b) CV curves. (c) Specific capacitances of electrodes calculated from GCD curves as a function of current density. (d) Schematic illustration of the synthesis process for p-HHB-Cu and np-HHB-Cu. Unit cell structures of HHB-Cu derived using. (e) Schematic synthesis of the CuPc(SH)$_8$ ligand and Ni$_2$[CuPcS$_8$] and the space-filling model of Ni$_2$[CuPcS$_8$]. (a)-(c) were reproduced with permission from ref 78. Copyright 2023 Wiley. (d) was reproduced with permission from ref 79. Copyright 2024 Wiley. (e) was adapted with permission from ref 80. Copyright 2024 American Chemical Society.

Feng group developed NH$_4$$^+$ hybrid supercapacitors (HSC) using a 2D *c*-MOF of Cu-HHB to immobilize iodine (Cu-HHB/I$_2$) as the cathode material (Fig. 8a).[78] Cu-HHB/I$_2$ features an excellent areal capacitance of 111.7 mF·cm^{-2} at 0.4 mA·cm^{-2}, shown in Fig 8b. Cu-O$_4$ nodes in Cu-HHB can act as both binding sites for iodine and redox-active sites. As shown in Fig. 8c, the synergy between CuO$_4$ and I$_2$ via redox reactions contributes to the high pseudocapacitance. In another example, as displayed in Fig. 8d, Bonaccorso and coworkers developed porous Cu-HHB through a surfactant-assisted method as negative electrodes with activated carbon as positive electrodes for hybrid supercapacitors.[79] The Cu-HHB based HSC exhibits high cell specific capacity (22.1 mA·h^{-1}·g^{-1} at 0.1 A·g^{-1}), and specific energy (15.55 Wh·kg^{-1}) with 77% cyclic stability. Combined charge storage mechanisms, including EDLC- and battery-type Faradic behavior, have been proposed as a result of the redox reaction of Cu^{2+} to Cu$^+$/Cu^0 from CuO$_4$ units and catechols to benzoquinones of the HHB ligands. Recently, Feng et al. synthesized a 2D *c*-MOF of Ni$_2$[CuPcS$_8$] (Fig. 8e) that displayed a high capacitance of 312 F·g^{-1} in non-aqueous supercapacitors with EDLC-type pseudocapacitive behavior.[80] The redox-active NiS$_4$ nodes maintain a localized lowest unoccupied molecular orbital (LUMO), which enhances the injected electrons responsible for the high capacitance.

Chang et al. designed and reported a 2D *c*-MOF of Ni-TTC, showing about 1.0 S·m^{-1}electrical conductivity, in which TTC

possess redox activity with *D*$_4$ symmetry.[81] The semiquinone ligand radicals together with Ni^{2+} sites, resulting in strong antiferromagnetic properties, ensured a gravimetric capacitance of 249 F·g^{-1} at 0.2 A·g^{-1}. Good electrical conductivity and a large surface area are beneficial for enhancing the EDL capacitance of 2D *c*-MOFs. The pseudocapacitance of 2D *c*-MOFs can be improved by embedding diverse redox-active substrates from ligands and metal ion nodes.

4.2 Batteries

Rechargeable batteries with high energy densities include lithium-ion batteries (LIBs) and the gradually rising generation of cost-effective and abundant metal ion batteries, such as sodium-ion batteries (SIBs), potassium-ion batteries (PIBs), zinc-ion batteries (ZIBs), next-generation lithium-sulfur (Li-S) batteries, and sodium iodine (Na-I$_2$) batteries. Electrode materials play a core role in batteries because of their reversible charge-discharge processes and complex electrochemical redox reactions. The outstanding merits of 2D *c*-MOFs, including multiple redox-active sites, superior electrical conductivity, regular channels, and remarkable durability, make them superior electrode materials for various batteries.

4.2.1 Lithium ion batteries. As commercialized batteries and electronics, LIBs exhibit high energy densities, large output voltages, and long cycling lifetimes. In recent decades, 2D *c*-MOFs have been widely investigated as advanced cathode materials in LIBs. Ni-HITP is the first 2D *c*-MOF used in LIBs reported by Nishihara in 2018.[82] Based on its unique redox properties and decent electrical conductivity, Ni-HITP showcased a specific capacity of (155 mAh^{-1} g^{-1}) and a high specific energy density (434 Wh kg^{-1} at 10 mA g^{-1}) with a multielectron-transfer and intercalation-mediated mechanism.

In 2020, we synthesized a redox-active Cu-HTQ MOF as cathode material for LIBs.[31] Cu-HTQ exhibited a large reversible capacity of 387 mAh^{-1} g^{-1} and a high energy density of 775 Wh kg^{-1} by the Li$^+$ insertion/extraction mechanism. Comprehensive spectroscopic techniques revealed redox reactions of one electron per Cu^{2+} ion and three electrons per coordinated unit. Prominent redox activity of both HTQ and copper ions occurred in the charge and discharge process, as shown in Fig. 9a, suggesting the rational design of effective 2D c-MOF-based cathode materials. Subsequently, we developed a pyrazine-based TPQG-Cu-MOF as the cathode material for LIBs (Fig. 9b).[83] TPQG-Cu-MOF displayed a reversible specific capacity of 150.2 mAh^{-1} g^{-1} at 20 mA g^{-1} with nearly 100% coulombic efficiency. The Li$^+$ insertion/extraction mechanism driven by the CuO$_2$ and pyrazine units was characterized by comprehensive *in-situ* spectroscopic investigations, as displayed in Fig. 9c. During the charge and discharge process, six lithium atoms and six electrons were extracted and acquired by TPQG-Cu-MOF (Fig. 9d).

Correlated studies employing redox-active ligands to construct 2D *c*-MOFs as cathode materials have also been reported. The highly conductive Cu-BHT revealed a capacity of 175 mAh^{-1} g^{-1} via a reversible four-electron reaction.[84] Cu-HHTQ joins nitrogen-rich tricycloquinzoline (TQ) and CuO$_4$ units, for which the synergistic effect results in a high capacity (657.6

mAh^{-1} g^{-1} at 600 mA g^{-1}). For the first time, TQ has been demonstrated to be a redox-active component of Li$^+$ ions.[43] Binary organic ligands with redox activity were used to construct a 2D *c*-MOF, Cu$_3$(HHTP)(HTQ), as reported by Bu and coworkers.[85] Aromatic rings and CuO$_4$ units were used for Li$^+$ ion storage, achieving a high specific capacity of 725.1 mAh^{-1} g^{-1} at 50 mA g^{-1}. Using CuO$_4$ units and C=N sites of the TAC (triazacoronene) ligand for Li$^+$ ion storage, Bu and coworkers reported a 2D *c*-MOF of Cu-TAC as anode materials, achieving a remarkable reversible capacity of 772.4 mAh g^{-1} at 300 mA g^{-1}, along with outstanding rate performance and long-term cyclability.[86] Fe-TABQ with two redox active centers from Fe ions and ligands, delivers a high capacity of 251.1 mAh g^{-1} at 50 mA g^{-1}, reported by Li group.[87] Furthermore, to construct dense redox-active sites, Li group also reported a one-dimensional Cu-MOF (DDA-Cu, where DDA = 1,5-Diamino-4,8-dihydroxy-9,10-anthracene-dione) as cathode materials for LIBs. The Cu-O$_3$ N units, through π-d conjugation, ensure structural robustness and high conductivity. The C=N bonds and Cu-O$_3$ N units serve as redox-active sites for Li$^+$ storage, delivering a high-rate capability of 192 mAh g^{-1} at 1 A g^{-1}. Furthermore, DDA-Cu demonstrates excellent performance when tested under lean electrolyte conditions with high mass loading.

Hexaazatriphenylene (HATN), with the redox activity of a nitrogen-rich heteroaromatic molecule, was utilized to synthesize a Cu-based 2D *c*-MOF of Cu-HATN.[89] The C=O bonds in CuO$_4$ units and C=N bonds in HATN establish the maximum number of active sites, together with regular channels for fast mass transfer and favorable electriconductivity. Cu-HATN demonstrates enhanced specific capacity of 763 mAh^{-1} g^{-1} at 300 mA g^{-1}. Similarly, 2D *c-MOF* of Cu-TAC with trazacoronene core displays an excellent reversible capacity (772.4 mAh^{-1} g^{-1} at 300 mA g^{-1}).[90] The C=N and C=O bonds from the TAC and CuO$_4$ units synergistically served as active sites for Li$^+$ ion storage.

Recently, Dong et al. designed a 2D *c*-MOF of Cu$_2$(N$_x$-OHPTP) (x=0, 1, 2) for dual-ion storage based on a nitrogen-variable π-conjugated octahydroxyphenanthrotriphenylene (OHPTP).[92] Cu$_2$(N$_2$-OHPTP), as a cathode, exhibited a large specific capacity of 53.8 mAh^{-1} g^{-1}. The nitrogen atoms in the skeleton of Cu$_2$(N$_x$-OHPTP) can regulate the electrical properties of narrower bandgaps and faster charge mobilities. Nitrogen can also serve as additional Li$^+$ ion adsorption sites and redox-active centers, favoring the CuO$_4$-nodes to adsorb Li$^+$ and Cl$^-$, resulting in a synergistic effect for enhanced dual-ion storage.

2D *c*-MOFs of M-TH5 (M = Mn, Co) with 3D extended structures featuring flower-like morphology were synthesized, in which TH5 contained a redox-active core of triptycene.[91] Mn-TH5 exhibits high initial capacity of 486.3 mAh^{-1} g^{-1} at 100 mA g^{-1} based on the TH5 and MnO$_4$ as dual redox centers. For future development, new ligands with rich redox-active sites integrated into 2D *c*-MOFs will induce particularly satisfactory performance, together with improved elucidation of the Li storage mechanism.

4.2.2 Sodium ion batteries. SIBs are widely verified as one promising alternative to LIBs, considered on the abundance (23600 ppm) with cheap price and low electrochemical potential (-2.71 V vs SHE). A heavier molar mass and larger ionic radius are critical

requirements for the pore structure and mass-transport ability of electrode materials. 2D *c*-MOFs, possessing adjustable pore and channel structures based on the size and symmetry of organic linkers, together with high electrical conductivity as well as highly dense redox-active sites from metal units and organic linkers, can effectively address the above problems.
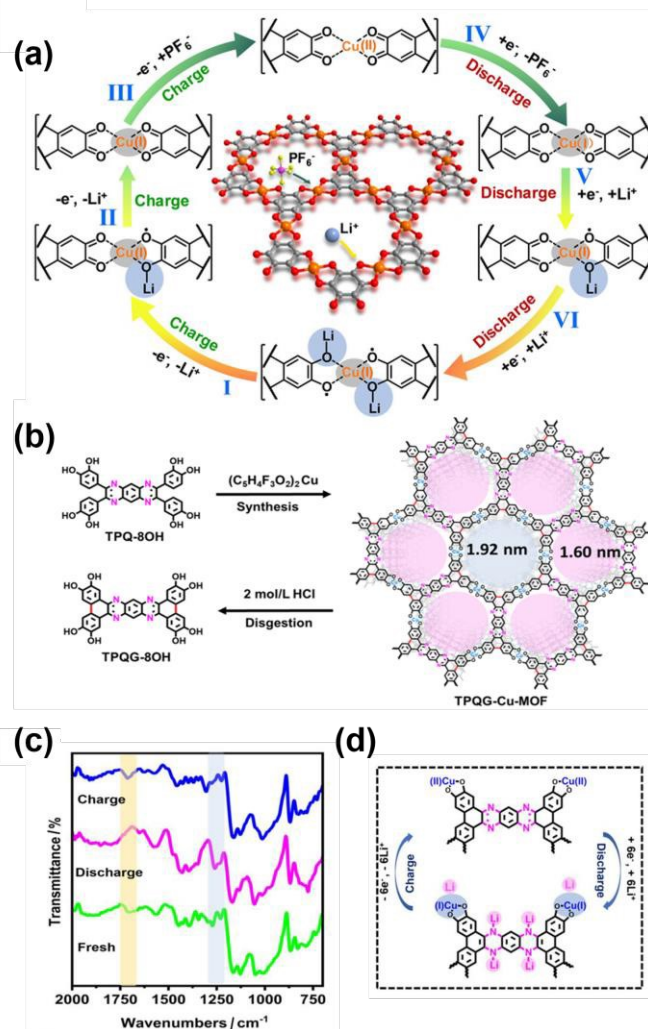

Fig. 9 (a) The evolution of electronic states of the repeating coordination unit of 2D Cu-THQ MOF during the charge/discharge process. (b) Schematic illustration of synthesis method of TPQG-Cu-MOF. (c) The ex-situ FT-IR TPQG-Cu-MOF electrode at different states for the lithium storing mechanism. (d) A schematic diagram of storing lithium ions mechanism. (a) was reproduced with permission from ref 31. Copyright 2020 Wiley. (b)-(d) were adapted with permission from ref 83. Copyright 2023 Wiley.

The first attempt of using 2D *c*-MOFs was Co-HAB, in which HAB featured the highest density of redox centers for a six-electron reaction.[93] Co-HAB can store three electrons and three sodium ions per HAB, achieving full availability of the redox centers in the HAB. The Co-HAB electrode exhibited a rate capability of 214 mAh g^{-1}. The Ni-TABQ reported by Wang et al. showed a 2D layer structure, providing two pathways along the polymer chain through Ni-N bonds and hydrogen bond direction for Na$^+$ ion diffusion and electron conduction.[94] The imines and

carbonyls in the conjugated benzene rings act as dual redox-active sites to insert and extract Na^+ ions. Ni-TABQ show excellent capacities of 469.5 and 345.4 mAh^{-1} g^{-1} at 100 mA·g^{-1} and 8 A·g^{-1}, respectively.

Using inactive Zn^{2+} ions and the redox-active ligand HHTP, Wang et al. synthesized a 2D c-MOF of Zn-HHTP.[40] Through successive redox reactions to store cations and anions, Zn-HHTP illustrated a highly reversible capacity (ca. 150 mAh^{-1} g^{-1} at 100 mA g^{-1}). After 1000 cycles manipulation, the capacity retention was maintained at 90%, which was superior to that of Cu-HHTP. For multi-redox sites, the Li group synthesized 2D c-MOFs of HATN-XCu (X=O/S) based on hexaazatrinaphthylene as an anode material for SIBs.[95] The dual redox sites of the repeating [CuX$_4$] units and C=N groups can lead to continuous multi-electron reactions, in which HATN-OCu has a reversible capacity of 500 mAh^{-1} g^{-1} at 100 mA g^{-1} and a rate performance of 151 mAh^{-1} g^{-1} at 5 A g^{-1}.
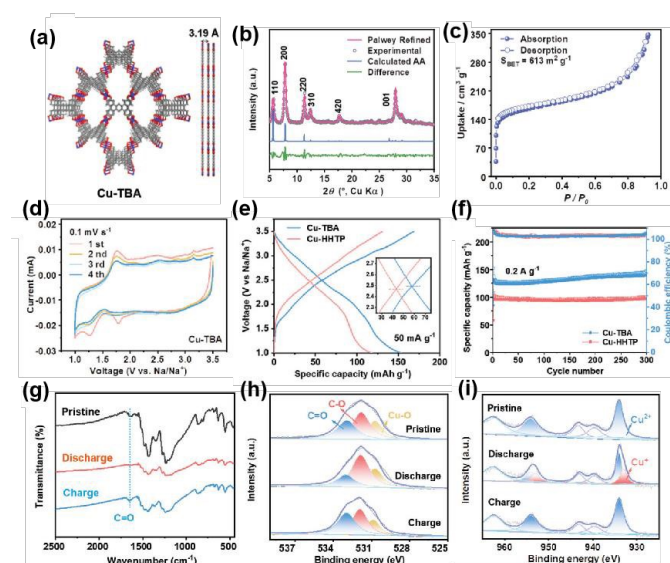

Fig. 10 (a) Structural model of Cu-TBA. (b) Experimental patterns, Pawley refined patterns, the difference between experimental and refined patterns, calculated pattern, and positions of reflections. (c) N$_2$ sorption isotherms. (d) CV curves at 0.1 mV s^{-1}. (e) GCD profiles at 50 mA g^{-1}. (f) Cycling stability at 0.2 A g^{-1}. (g-i) FT-IR spectra and high-resolution XPS spectra of O 1s and Cu 2p at different states of the initial cycle. Reproduced with permission from ref 96. Copyright 2024 Wiley.

Our group introduced a large conjugated ligand of octahydroxyteterabenzoanthracene (8OH-TBA) with a narrow energy gap to construct a 2D c-MOF of Cu-TBA with rhombic topology (Fig. 10a-10b).[96] As displayed in Fig. 10c, Cu-TBA exhibits a metallic band structure with a high specific surface area of 613 m^2 g^{-1}. In Na^+ ions storage, Cu-TBA demonstrates decent reversible capacity of 153.6 mAh^{-1} g^{-1} at 50 mA g^{-1} and superior cyclability (Fig. 10d-10f), outperforming the hexagonal counterpart of Cu-HHTP. The mechanism of Na^+ ions storage involves tree-step reactions, including a single electron reduction of Cu^{2+}/Cu^+ and successive two electron process of C=O/C-O reduction, shown in Fig. 10g-10i. Subsequently, anion and cation co-storage in SIBs was revealed for the first time using Ni$_3$(HATQ)$_2$ as a bipolar active material, based on a p-type

ligand rich in nitrogen and deficient in electrons.[97] Ni$_3$(HATQ)$_2$ showed a Brunauer-Emmett-Teller (BET) surface area of 513 m^2 g^{-1} with a mesopore size of 2.24 nm and a conductivity of 2.12 mS·m^{-1}. The reversible capacity of Ni$_3$(HATQ)$_2$ is 115.1 mAh^{-1} g^{-1} with fine rate performance of 77.1 mAh^{-1} g^{-1} at 2 A g^{-1} and long-time cycling durability. Comprehensive characterization techniques revealed that the C=N bonds of the coordinated center tended to store Na^+ ions, and PF_6^- ions were more easily bonded to the nitrogen atoms of the TQ ligand. Ultimately, the release of synergistic effects on the maximum degree of different redox-active components is pivotal, for which the rational design of 2D c-MOFs is essential.

4.2.3 Zinc ion batteries. The advantages of high water compatibility, nontoxicity, low cost, and nonflammability make zinc as an ideal candidate for anode materials in batteries.[98] Aqueous ZIBs feature high power and energy densities owing to their multiple ionic charge transport carriers. Zn^{2+} ions can be inserted and deserted in the nanochannels and interlamination of 2D c-MOFs, indicating that compatible pore sizes and layer spacings for zinc ion accommodation are key factors for improving the performance of ZIBs.

The first use of 2D c-MOFs in ZIBs was for Cu$_3$(HTTP)$_2$, as reported by the Stoddart group.[99] Cu$_3$(HTTP)$_2$ delivers a capacity of 124.4 mAh^{-1} g^{-1} at 4000 mA g^{-1}, originating from a main pseudocapacitive charge-storage mechanism from two redox centers of Cu^{2+} and quinoidal units. Liang et al. reported a 2D c-MOF of Cu-BTA-H as the cathode materials for ZIBs.[100] The dual redox mechanisms of Cu^{2+}/Cu^+ via a one-electron redox reaction and C=N/C-N via a two-electron redox reaction resulted in an enhanced reversible capacity of 330 mAh^{-1} g^{-1} at 2000 mA g^{-1}.

To integrate multiple redox-active components into the 2D c-MOFs, we tailored a multitopic catechol ligand based on an anthraquinone core to synthesize a novel Cu-TBPQ MOF.[101] Cu-TBPQ was synthesized using flexible nonplanar ligand of 8OH-TBPQ and Cu^{2+} under solvothermal conditions through one-pot cyclodehydrogenation and coordination reaction of 8OH-TBPQ and Cu^{2+} simultaneously. Cu-TBPQ MOF exhibited good stability in water, common organic solvents such as DMF and acetone, and 3 M NaOH aqueous solution. As a ZIB cathode, Cu-TBPQ MOF achieved a high specific capacity of 371.2 mAh^{-1} g^{-1} at 50 mA g^{-1} with superior rate performance and stability, with nearly 88% retention of the initial capacity after 500 cycles at 2A g^{-1}. The quinone moieties largely induced dense redox active sites, including [CuO$_4$] units and quinone moieties, enabling the storage of Zn^{2+} ions in Cu-TBPQ MOF.

A large surface area and proper pore size are essential for electrode materials in aqueous dual-ion batteries. To address this need, we developed two 2D c-MOFs: PA-TAPA-Cu-MOF and PA-PyTTA-Cu-MOF.[102] PA-TAPA-Cu-MOF exhibits the largest pore size of 3.9 nm among the reported 2D c-MOFs. These two MOFs are conducted as cathode materials for polyiodides storage for the first time. PA-TAPA-Cu-MOF displays higher specific capacity (423.4 mAh g^{-1} after 100 cycles at 1.0 A g^{-1}) than that of PA-PyTTA-Cu-MOF. In addition to the large pores that facilitate the storage and transport of I$^-$/I$_3^-$, the nitrogen atoms and CuO$_4$ centers also play a crucial role in anchoring I$_3^-$.

4.2.4 Potassium ion batteries. The merits of potassium ions, such as Earth's abundance, low cost, and high security, make

potassium ion batteries (PIBs) as promising alternative to LIBs. The device configuration and manufacturing process of PIBs are analogical to those of LIBs. Currently, the existing challenges of limited capacity and slow kinetics originating from the much larger radius of K+ urgently need to be solved by synthesizing proper materials for K+ accumulation. Organic materials are superior to inorganic materials owing to their designable and flexible structures and environmental friendliness. 2D *c*-MOFs stand out as an inimitable class of organic polymers, in which the periodic and multiple active sites are beneficial for storing K+ ions. Meanwhile, the delocalization of electrons in the overall framework can improve the conductivity and stability, and 2D *c*-MOFs can be used as promising cathode materials for PIBs.
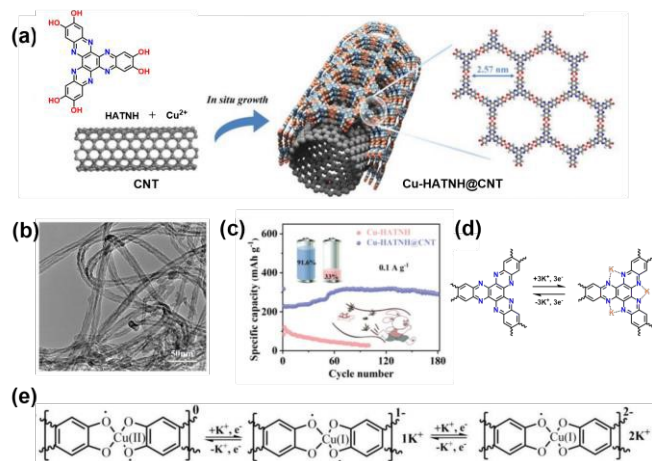

Fig. 11 (a) Schematic of the synthesis of Cu-HATNH@CNT. (b) TEM images of Cu-HATNH@CNT. (c) Cycling performance of CuHATNH@CNT at 0.1 A g^{-1}. (d) Schematic of the K+ storage process in the HATNH units. (e) Schematic of the K+ storage process in the [CuO$_4$] units. Adapted with permission from ref 100. Copyright 2024 Wiley.

Conjugation and topology engineering are essential for adjusting the electrochemical properties of 2D *c*-MOFs. Wang et al. utilized the 2D *c*-MOF of Cu-TBA-MOF with different topologies but same conjugated tetrabenzoanthracene (TBA) aromatic core for PIBs using a topology engineering strategy.[103] The rhombus topological *sql*-Cu-TBA-MOF shows extended π-conjugation, larger specific surface area and better structural stability than the kagome analogue (*kgm*-Cu-TBA-MOF), which can expose more active centers and faster diffusion of K+ ions, resulting in better electrochemical performance. *sql*-Cu-TBA-MOF reveals a high specific discharge capacity of 178.4 mAh g^{-1} at 0.2 A g^{-1} and an excellent long-term cycle stability (more than 9,000 cycles at 10.0 A g^{-1}). Full PIBs constructed using dipotassium terephthalate as anode and sql-Cu-TBA-MOF as cathode, delivers a reversible discharge specific capacity of 146.6 mAh g^{-1} at 0.1 A g^{-1}, which in series can charge the smart phone. Moreover, *sql*-Cu-TBA-MOF exhibited good performance at a low temperature of -20 °C. The reversible redox reactions of C=O/C-O-K and Cu^{2+}/Cu$^+$ were verified as K+ storage mechanisms. This work sticks out the importance of topological structures and conjugation for 2D *c*-MOFs in energy storage devices.

Multiple active sites from the coordination units and unsaturated bonds of ligands can be integrated into 2D *c*-MOFs with promising electrochemical performance for PIBs. Zhu group reported

the first application of a 2D *c*-MOF (Cu-HATNH) with dual active centers combined with carbon nanotubes (Cu-HATNH@CNT) as a cathode material for PIBs.[104] Cu-HATNH@CNT show a core-shell structure with Cu-HATNH grown *in situ* on CNT, as shown in Fig. 11a-11b. Carbon nanotubes can not only improve the conductivity but also enlarge the layer space and pore size, accelerating the electron transfer and K+ migration and diffusion. Cu-HATNH@CNT displays a high initial capacity of 317.5 mA h g^{-1} at 0.1 A g^{-1}, remarkable rate capacity of 147.1 mA h g^{-1} at 10 A g^{-1}, and outstanding long-term cycling durability. Moreover, Cu-HATNH@CNT displayed a high invertible capacity of 290.4 mA h g^{-1} and capacity retention of 91.6% after 180 cycles (Fig. 11c). The unsaturated bonds of C=N were verified as the active sites that bind K+. The [CuO$_4$] units can also store K+ through redox reactions (Fig.11d-11e). The abundant C=N sites from HATNH and unsaturated [CuO$_4$] units act synergistically to store K+ ions at a high utilization rate. This study proposes a novel strategy to design 2D *c*-MOFs with high capacity as organic cathode materials in secondary batteries.

2D *c*-MOFs can also be used as anode electrode materials in PIBs, such as HAN-Cu-MOF reported by Li group.[105] The nitrogen-rich ligands and CuO$_4$ nodes with π-d conjugation endow the HAN-Cu-MOF with multiple redox-active sites and robust stability to efficiently store potassium ions at high temperatures. At 60 °C, HAN-Cu-MOF delivered a high initial capacity of 455 mAh g^{-1} and extraordinary cyclability with 96.7% capacity retention after 1600 cycles. The CuO$_4$ units and C=N functional groups contribute the majority of redox-active sites, which are responsible for the high reversible capacity. The characteristics of periodic porous conjugated frameworks guarantee fast charge transport and excellent cycle durability. This study provides a new perspective for designing highly efficient battery electrode materials under high-temperature conditions based on coordination chemistry strategies.

4.2.5 Magnesium/Ammonium ion batteries and Lithium-Sulfur batteries. Magnesium ion batteries (MIBs) present promising alternatives to lithium-ion batteries due to the abundant availability of magnesium and its high theoretical capacity (up to 3,833 mAh/cm³). However, a significant challenge remains in identifying suitable cathode materials, primarily due to the high diffusion energy barriers of Mg^{2+} in most crystalline materials. This issue can be addressed by utilizing redox-active materials as conversion-type cathodes. 2D *c*-MOFs, with their rich redox-active components derived from metal nodes and ligands, can be ingeniously designed for use as cathode materials in MIBs. Wang et al. reported a sulfur-functionalized 2D *c*-MOF, Cu-S$_5$HHTP, as a cathode material for Mg^{2+} storage.[106] Cu-S$_5$HHTP exhibits a high capacity of approximately 500 mAh g^{-1} and superior cyclability. Following the insertion and extraction of Mg^{2+}, Cu-S$_5$HHTP undergoes structural transformation, resulting in disrupted long-range order while maintaining its 2D crumpled sheet structure. The sulfur functionality enhances the capacity by generating abundant redox-active sites.

Ammonium ion batteries (AIBs) represent a promising segment of low-cost energy storage systems, offering advantages such as environmental sustainability and extended lifespan. However, they face the challenge of slow diffusion kinetics. 2D *c*-MOFs can facilitate rapid reaction kinetics, alongside high electrical conductivity and abundant redox-active components, making them strong candidates for cathode materials in AIBs. Utilizing a heterogeneous ligand

approach, Xu and colleagues synthesized the 2D Cu-HHTP-THBQ.[107] Through electron delocalization regulated by the heteroligand and a hydrogen bond cage mechanism, the full battery demonstrates a high specific energy density of 211.84 Wh kg^{-1}. The presence of double redox-active sites from Cu cations and heteroligand anions contributes to a significant specific capacity.

Lithium-sulfur batteries (LSBs) are regarded as one of the most promising next-generation battery technologies due to their high theoretical energy density and the abundance of sulfur. However, the insulating nature of sulfur, coupled with the notorious shuttle effect and volume strain of the electrode structure, significantly limits the practical applications of LSBs. 2D c-MOFs, with their excellent intrinsic electrical conductivity, can serve as ideal modified separator layers in LSBs. The Zhu group employed the smallest π-conjugated hexaaminobenzene (HAB) ligand to construct the 2D c-MOF Ni-HAB, which was further hybridized with carbon nanotubes (CNT) to create Ni-HAB@CNT.[108] As a modified separator, Ni-HAB@CNT achieves an areal capacity of 6.29 mAh cm^{-2} at a high sulfur loading of 6.5 mg cm^{-2}, under an electrolyte-to-sulfur ratio of 5 μL mg^{-1}. The Ni-N$_4$ chemisorption sites, combined with micropores, effectively enhance sulfur affinity and mitigate the shuttle effect.

5. Summary and outlook

In this review, we summarize the recent key progress of 2D c-MOFs in electrochemical energy conversion and storage systems, including electrocatalysis (ORR, OER, HER, CO$_2$RR, and NRR), supercapacitors, and metal-ion batteries (Li, Na, Zn and K). The synergistic effect of the metal nodes and ligands with redox-active sites was the focus of this article. Incorporated with redox ligands, 2D c-MOFs can achieve the maximum number of active sites, mainly involving unsaturated covalent bonds, such as C=O and C=N, etc. The intrinsic electrical conductivity, high porosity with regular channels, and rich active components make 2D c-MOF multifunctional materials suitable for gas sensing, electronics, electrochemical energy conversion, and storage applications. Considering the booming background of 2D c-MOFs, the remaining challenges must be addressed for their practical application.

First, more diverse novel redox ligands are expected to be introduced into the 2D c-MOFs. Organic ligands can usually determine the topology, pore structures, and redox activity of 2D c-MOFs, which influence the functions of specific structures based on structure-function relationships. The rational design of innovative organic ligands can establish perfect synergy between various components, thereby significantly improving the performance of electrochemical devices. Meantime, more metal ions, such as Ti, V, Cr and Mo are needed to import in 2D c-MOFs to explore more intriguing applications. Furthermore, machine learning and DFT calculations can be used to screen and evaluate the properties of 2D c-MOFs using systematic models, which can aid the design and synthesis of tailor-made 2D c-MOFs.

Second, the crystallinity of 2D c-MOFs should be improved for large single crystals or single-crystalline thin films. Polycrystalline powders are commonly used and show inferior activity compared to theoretical expectations, in which the

disordered structures largely influence the long-range pathways of charge and mass transport. However, structure-property relationships cannot be elucidated at the molecular level. The use of nonplanar ligands to construct 2D c-MOFs is a straightforward and accessible strategy for obtaining high-quality crystals with multiple functions.

Third, the applications of 2D c-MOFs in new fields should be developed. For example, there have been few reports of biomass catalysis and sensing.[109-110] The application of 2D c-MOFs in interdisciplinary fields is promising, but remains less exploited. Incorporating guest molecules such as carbon nanotubes, cationic clusters, and polyoxometalates to contruct 2D c-MOF-based hybrids can offer more intriguing functions for various applications. For example, 2D c-MOF (Cu-HATNH) with dual-active centers was anchored on carbon nanotubes, which were used as cathode materials for PIBs.[104]

Fourth, the real active sites of the 2D c-MOFs in electrocatalytic reactions should be investigated in detail. In particular, high-valence metal oxides or hydroxides, such as MOOH derived from metal nodes, are considered as the real active sites for oxidation reactions. Defects and grain boundaries, which can be introduced through chemical modification, are confirmed to be highly active sites. For example, peripheral defects in Cu-HHTP are related to the enhanced catalytic performance of CO$_2$RR.[104] Advanced *in situ* characteristic techniques should be developed to monitor the transformation of active components during the dynamic catalytic process and understand the mechanism of structural reconstruction.

Last but not the least, for practical applications, economic feasibility must be considered and assessed to achieve mass production. Low-cost raw materials and advanced synthetic techniques for industrial scalability are prerequisites for practical applications that should be widely studied in the future. In general, 2D c-MOFs with multiple functions are still in their infancy with various emerging applications. This review is expected to arouse more research interest regarding the maximum utilization of the active components in 2D c-MOFs.

Author contributions

Z. M. Su and L. Chen conceptualized the review. X. Li, X. Su and T. Su wrote and edited the review.

Conflicts of interest

There are no conflicts to declare.

Acknowledgements

References

1   A. Schoedel, Z. Ji, O. M. Yaghi, *Nat. Energy*, 2016, **1**, 16034.

2   L. Chen, X. Xu, W. Yang, J. Jia, *Chin. Chem. Lett.,* 2020, **31**, 626-634.

3   P. Zhang, F. Wang, M. Yu, X. Zhuang, X. Feng, *Chem. Soc. Rev.*, 2018, **47**, 7426-7451.

4   J. Li, X. Gao, L. Zhu, M. N. Ghazzal, J. Zhang, C. H. Tung, L. Z. Wu, *Energy. Environ. Sci.*, 2020, **13**, 1326-1346.

5   Q. Fu, J. Han, X. Wang, P. Xu, T. Yao, J. Zhong, W. Zhong, S. Liu, T. Gao, Z. Zhang, L. Xu, B. Song, *Adv. Mater.*, 2021, **33**, 1907818.

6   I. Khan, N. Baig, S. Ali, M. Usman, S. A. Khan, K. Saeed, *Energy Storage Mater.*, 2021, **35**, 443-469.

7   G. Wu, P. Zelenay, *Nat. Rev. Mater.*, 2024, **9**, 643-656.

8   H. Su, M. A. Soldatov, V. Roldugin, Q. Liu, *eScience*, 2022, **2**, 102-109.

9   T. Wang, X. Cao, L. Jiao, *eScience,* 2021, **1**, 69-74.

10   J. Li, H. M. Yin, X. B. Li, E. Okunishi, Y. L. Shen, J. He, Z.-K. Tang, W. X. Wang, E. Yucelen, C. Li, Y. Gong, L. Gu, S. Miao, L. M. Liu, J. Luo, Y. Ding, *Nat. Energy*, 2017, **2**, 17111.

11   M. Liu, Y. Pang, B. Zhang, P. De Luna, O. Voznyy, J. Xu, X. Zheng, C. T. Dinh, F. Fan, C. Cao, F. P. de Arquer, T. S. Safaei, A. Mepham, A. Klinkova, E. Kumacheva, T. Filleter, D. Sinton, S. O. Kelley, E. H. Sargent, *Nature*, 2016, **537**, 382-386.

12   Z. Li, Y. J Chen, S. Ji, Y. Tang, W. Chen, A. Li, J. Zhao, Y. Xiong, Y. Wu, Y. Gong, T. Yao, W. Liu, L. Zheng, J. Dong, Y. Wang, Z. Zhuang, W. Xing, C. He, C. Peng, W. Cheong, Q. Li, M. Zhang, Z. Fu, X. Gao, W. Zhu, J. Wan, J. Zhang, L. Gu, S. Wei, P. Hu, J. Luo, J. Li, C. Chen, Q. Peng, X. Duan, Y. Huang, X. Chen, D. Wang, Y. Li, *Nat. Chem.*, 2020, **12**, 764-772.

13   J. Zhang, G. Chen, K. Mullen, X. L. Feng, *Adv. Mater.*, 2018, **30**, 1800528.

14   H. Furukawa, K. E. Cordova, M. O'Keeffe, O. M. Yaghi, *Science*, 2013, **341**, 1230444.

15   H. Zhang, J. Nai, L. Yu, X. W. Lou, *Joule*, 2017, **1**, 77-107.

16   D. Xiang, X. Bo, X. Gao, C. Du, P. Li, L. Zhu, W. J. Chen, *Colloid Interface Sci.*, 2019, **534**, 655-664.

17   C. Du, Y. Gao, J. Wang, W. Chen, *J. Mater. Chem. A*, 2020, **8**, 9981-9990.

18   M. Wang, R. H. Dong, X. L. Feng, *Chem. Soc. Rev.*, 2021, **50**, 2764-2793.

19   S. Wu, Y. Lin, J. Liu, W. Shi, G. Yang, P. Cheng, *Adv. Funct. Mater.*, 2018, **28**, 1707169.

20   W. Hao, D. Chen, Y. Li, Z. Yang, G. Xing, J. Li, L. Chen, *Chem. Mater.*, 2019, **31**, 8100-8105.

21   X. Yan, H. Liu, Y. Li, W. Chen, T. Zhang, Z. Zhao, G. Xing, L. Chen, *Macromolecules*, 2019, **52**, 7977-7983.

22   J. Hou, A. Gómez, A. Krajnc, A. McCaul, S. Li, A. M. Bumstead, A. F. Sapnik, Z. Deng, R. Lin, P. A. Chater, D. S. Keeble, D. A. Keen, D. Appadoo, B. Chan, V. Chen, G. Mali, T. D. Bennett, *J. Am. Chem. Soc.*, 2020, **142**, 3880-3890.

23   A. E. Thorarinsdottir, T. D. Harris, *Chem. Rev.*, 2020, **120**, 8716-8789.

24   M. Savage, Y. Cheng, T. L. Easun, J. E. Eyley, S. P. Argent, M. R. Warren, W. Lewis, C. Murray, C. C. Tang, M. D. Frogley, G. Cinque, J. Sun, S. Rudic´, R. T. Murden, M. J. Benham, A. N. Fitch, A. J. Blake, A. J. Ramirez-Cuesta, S. Yang, M. Schrçder, *Adv. Mater.*, 2016, **28**, 8705-8711.

25   M. Yu, R. H. Dong, X. L. Feng, *J. Am. Chem. Soc.*, 2020, **142**, 12903-12915.

26   H. Zhong, M. Wang, G. Chen, R. H. Dong, X. L. Feng, *ACS Nano,* 2022, **16**, 1759-1780.

27   L. Lin, Q. Zhang, Y. Ni, L. Shang, X. Zhang, Z. Yan, Q. Zhao, and J. Chen, *Chem*, 2022, **8**, 1822-1854.

28   J. Liu, X. Song, T. Zhang, S. Liu, H. Wen, L. Chen, *Angew. Chem. Int. Ed.*, 2021, **60**, 5612-5624.

29   M, Zhao, S, Tong, *Energy Fuels*, 2024, **38**, 13796-13818.

30   L. Sun, M. G. Campbell, M. Dincǎ, *Angew. Chem. Int. Ed.*, 2016, **55**, 3566-3579.

31   Q. Jiang, P. Liu, J. Xiong, Z. Xie, Q. Wang, X. Q. Yang, E. Hu, Y. Cao, J. Sun, Y. Xu, L Chen, *Angew. Chem., Int. Ed.*, 2020, **59**, 5273-5277.

32   Z. Meng, A. Aykanat, K. A. Mirica, *J. Am. Chem. Soc.*, 2019, **141**, 2046-2053.

33   J. Park, A. C. Hinckley, Z. Huang, D. Feng, A. A. Yakovenko, M. Lee, S. Chen, X. Zou, Z. Bao, *J. Am. Chem. Soc.*, 2018, **140**, 14533-14537.

34   J. Liu, Y. Zhou, Z. Xie, Y. Li, Y. Liu, J. Sun, Y. Ma, O. Terasaki, L. Chen, *Angew. Chem. Int. Ed.*, 2020, **59**, 1081-1086.

35   R. Dong, Z. Zhang, D. C. Tranca, S. Zhou, M. Wang, P. Adler, Z. Liao, F. Liu, Y. Sun, W. Shi, Z. Zhang, E. Zschech, S. C. B. Mannsfeld, C. Felser, X. Feng, *Nat. Commun.*, 2018, **9**, 2637.

36   M. Hmadeh, Z. Lu, Z. Liu, F. Gándara, H. Furukawa, S. Wan, V. Augustyn, R. Chang, L. Liao, F. Zhou, E. Perre, V. Ozolins, K. Suenaga, X. Duan, B. Dunn, Y. Yamamto, O. Terasaki, O. M. Yaghi, *Chem. Mater.*, 2012, **24**, 3511-3513.

37   H. T. B. Pham, J. Y. Choi, M. Stodolka, J. Park, *Acc. Chem. Res.*, 2024, **57**, 580-589.

38   J. Liu, G. Xing, L. Chen, *Acc. Chem. Res*., 2024, **57**, 1032-1045.

39   X. Su, Z. Zhong, X. Yan, Y. Xu, T. Zhang, Y. Ma, L. Chen, *J. Am. Chem. Soc.*, 2024, **146**, 9036-9044.

40   Y. Chen, Q. Zhu, K. Fan, Y. Gu, M. Sun, Z. Li, C. Zhang, Y. Wu, Q. Wang, S. Xu, J. Ma, C. Wang, W. Hu, *Angew. Chem. Int. Ed.*, 2021, **60**, 18769-18776.

41   X. Yan, J. Chen, X. Su, J. Zhang, C. Wang, H. Zhang, Y. Liu, L. Wang, G. Xu, L. Chen, *Angew. Chem. Int. Ed.*, 2024, **63**, e202408189.

42   J. Liu, Dan Yang, Y. Zhou, G. Zhang, G. Xing, Y. Liu, Y. Ma, O. Terasaki, S. Yang, L. Chen, *Angew. Chem. Int. Ed.*, 2021, **60**, 14473-14479.

43   J. Yan, Y. Cui, M. Xie, G. Yang, D. Bin, D. Li, *Angew. Chem. Int. Ed.*, 2021, **60**, 24467-24472.

44   B. C. H. Steele, A. Heinzel, *Nature*, 2001, **414**, 345-352.

45   F. Y. Cheng, J. Chen, *Chem. Soc. Rev.*, 2012, **41**, 2172-2192.

46   A. Schneemann, R. Dong, F. Schwotzer, H. Zhong, I. Senkovska, X. Feng, S. Kaskel, *Chem. Sci.*, 2021, **12**, 1600-1619.

47   L. Guo, J. Sun, J. Wei, Y. Liu, L. Hou, C. Yuan, *Carbon Energy*, 2020, **2**, 203-222.

48   E. M. Miner, T. Fukushima, D. Sheberla, L. Sun, Y. Surendranath, M Dincǎ, *Nat. Commun.*, 2016, **7**, 10942.

49   H. Zhong, K. H. Ly, M. Wang, Y. Krupskaya, X. Han, J. Zhang, J. Zhang, V. Kataev, B. Büchner, I. M. Weidinger, S. Kaskel, P. Liu, M. Chen, R. Dong, X. Feng, *Angew. Chem. Int. Ed.*, 2019, **58**, 10677-10682.

50   E. M. Miner, L. Wang M. Dincǎ, *Chem. Sci.*, 2018, **9**, 6286-6291.

Chemical Science

Journal Name

ARTICLE

51 E. M. Miner, S. Gul, N. D. Ricke, E. Pastor, J. Yano, V. K. Yachra, T. V. Voorhis, M. Dincă, *ACS Catal.*, 2017, **7**, 7726-7731.

52 J. Park, Z. Chen, R. A. Flores, G. Wallnerström, A. Kulkarni, J. K. Nørskov, T. F. Jaramillo, Z. Bao, *ACS Appl. Mater. Interfaces*, 2020, **12**, 39074-39081.

53 A. M. Dominic, Z. Wang, A. Kuc, P. Petkov, K. H. Ly, T. L. H. Pham, M. Kutzschbach, Y. Cao, J. Bachmann, X. Feng, R. Dong, I. M. Weidinger, *J. Phys. Chem. C*, 2023, **127**, 7299-7307.

54 X. Wei, C. Jiang, H. Xu, Y. Ouyang, Z. Wang, C. Lu, X. Lu, J. Pang, F. Dai, X. H. Bu, *ACS Catal.*, 2023, **13**, 15663-15672.

55 L. Wei, M. D. Hossain, G. Chen, G. A. Kamat, M. E. Kreider, J. Chen, K. Yan, Z. Bao, M. Bajdich, M. Burke Stevens, T. F. Jaramillo, *J. Am. Chem. Soc.*, 2024, **146**, 13377-13390.

56 C. Li, L. Shi, L. Zhang, P. Chen, J. Zhu, X. Wang Y. Fu, *J. Mater. Chem. A*, 2020, **8**, 369-379.

57 D. Xing, Y. Wang, P. Zhou, Y. Liu, Z. Wang, P. Wang, Z. Zheng, H. Cheng, Y. Dai, B. Huang, *Appl. Catal. B Environ.*, 2020, **278**, 119295.

58 J. Yang, Z. Feng, Y. Wang, J. Huang, C. Xu, H. Li, *ACS Appl. Nano Mater.*, 2024, **7**, 18881-18888.

59 Y. Lian, W. Yang, C. Zhang, H. Sun, Z. Deng, W. Xu, L. Song, Z. Ouyang, Z. Wang, J. Guo, Y. Peng, A*ngew.Chem. Int. Ed.*, 2020, **59**,286-294.

60 S. S. Shinde, C. H. Lee, J. Jung, N. K. Wagh, S. Kim, D. Kim, C. Lin, S. U. Lee and J. Lee, *Energy Environ. Sci.*, 2019,**12**, 727-738.

61 L. Hu, F. F. Wang, Y. Jing, *J. Phys. Chem. Lett.*, 2023, **14**, 11429-11437.

62 X. Wei, S. Cao, S. Cheng, C. Lu, X. Chen, X. Lu, X. Chen, F. Dai, *ACS Materials Lett.*, 2024, **6**, 3496-3504.

63 A. J. Clough, J. W. Yoo, M. H. Mecklenburg, S. C. Marinescu, *J. Am. Chem. Soc.*, 2015, **137**, 118-121.

64 P. Das, B. Ball, P. Sarkar, *ACS Catal.*, 2023, **13**, 16307-16317.

65 Y. Lu, H. Zhong, J. Li, A. M. Dominic, Y. Hu, Z. Gao, Y. Jiao, M. Wu, H. Qi, C. Huang, L. J. Wayment, U. Kaiser, E. Spiecker, I. M. Weidinger, W. Zhang, X. L. Feng, R. H. Dong, *Angew. Chem. Int. Ed.*, 2022, **61**, e202208163.

66 D. Yang, X. Wang, *SmartMat.*, 2022, **3**, 54-67.

67 H. X. Zhong, M. Ghorbani-Asl, K. H. Ly, J. C. Zhang, J. Ge, M. C. Wang, Z. Q. Liao, D. Makarov, E. Zschech, E. Brunner, I. M. Weidinger, J. Zhang, A. V. Krasheninnikov, S. Kaskel, R. H. Dong, X. L. Feng, *Nat Commun*, 2020, **11**, 1409.

68 Y. Liu, S. Li, L. Dai, J. Li, J. Lv, Z. Zhu, A. Yin, P. Li, B. Wang, *Angew. Chem. Int. Ed.*, 2021, **60**, 16409-16415.

69 Z. Zhao, J. Huang, P. Liao, X. Chen, *J. Am. Chem. Soc.*, 2023, **145**, 26783-26790.

70 W. Xiong, X. Cheng, T. Wang, Y. S. Luo, J. Feng, S. Y. Lu, A. M. Asiri, W. Li, Z. J. Jiang, X. P. Sun, *Nano Res*, 2020, **13**, 1008-1012.

71 J. Zhang, X. Zhu, W. Geng, T. Li, M. Li, C. Fang, X. Shan, Y. Li, Y. Jing, *J. Energy. Chem.*, 2021, **61**, 71-76.

72 A. Maibam, I. B. Orhan, S. Krishnamurty, S. P. Russo, R. Babarao, *ACS Appl. Mater. Interfaces*, 2024, **16**, 8707-8716.

73 Z. Xiong, Z. Xu, A. Y. Bao, W. Sheng, J. Zhan, *ACS Appl. Nano Mater.*, 2024, **7**, 4220-4227.

74 X. Huang, S. Zhang, L. Liu, L. Yu, G. Chen, W. Xu, D. Zhu, *Angew. Chem., Int. Ed.*, 2018, **57**, 146-150.

75 D. Sheberla, J. C. Bachman, J. S. Elias, C. Sun, Y. S. Horn, M. Dincă, *Nat. Mater.*, 2017, **16**, 220-224.

76 D. Feng, T. Lei, M. R. Lukatskaya, J. Park, Z. Huang, M. Lee, L. Shaw, S. Chen, A. A. Yakovenko, A. Kulkarni, J. Xiao, K. Fredrickson, J. B. Tok, X. Zou, Y. Cui, Z. Bao, *Nat. Energy*, 2018, **3**, 30-36.

77 J. Zhao, T. Zhang, J. Ren, Z. Zhao, X. Su, W. Chen, L. Chen, *Chem. Commun.*, 2023, **59**, 2978-2981.

78 M. Gao, Z. Wang, Z. Liu, Y. Huang, F. Wang, M. Wang, S. Yang, J. Li, J. Liu, H. Qi, P. Zhang, X. Lu, X. L. Feng, *Adv. Mater.*, 2023, **35**, 2305575.

79 A. Bagheri, S. Bellani, H. Beydaghi, Z. Wang, A. Morag, M. I. Zappia, J. K. P, S. Vaez, V. Mastronardi, A. Gamberini, S. B. Thorat, M. Abruzzese, R. H. Dong, L. Pasquale, M. Yu, X. L. Feng, F. Bonaccorso, *ChemSusChem*, 2024, e202401454.

80 P. Zhang, M. Wang, Y. Liu, Y. Fu, M. Gao, G. Wang, F. Wang, Z. Wang, G. Chen, S. Yang, Y. Liu, R. H. Dong, M. Yu, X. Lu, X. L. Feng, *J. Am. Chem. Soc.*, 2023, **145**, 6247-6256.

81 Z. Chang, M. Zhu, Y. Sun, F. He, Y. Li, C. Ye, Y. Jin, Z. Li, W. Xu, *Adv. Funct. Mater.*, 2023, **33**, 2301513.

82 K. Wada, K. Sakaushi, S. Sasaki, H. Nishihara, *Angew. Chem. Int. Ed.*, 2018, **57**, 8886-8890.

83 X. Sun, X. Yan, K. Song, T. Zhang, Z. Yang, X. Su, W. Chen, L. Chen, *Chin. J. Chem.*, 2023, **41**, 1691-1696.

84 Z. Wu, D. Adekoya, X. Huang, M. J. Kiefel, J. Xie, W. Xu, Q. Zhang, D. Zhu, S. Zhang, *ACS Nano*, 2020, **14**, 12016-12026.

85 J. C. Yin, Y. Q. Zhang, Z. G. Li, M. R. Cheng, M. Liu, W. Li, N. Li, X. H. Bu, *Sci China Mater*, 2023, **66**, 4566-4574.

86 J. C. Yin, X. Lian, Z. G. Li, M. R. Cheng, M. Liu, J. Xu, W. Li, Y. H. Xu, N. Li, X. H. Bu, *Adv. Funct. Mater.*, 2024, **34**, 2403656.

87 J. R. Geng, Y. X. Ni, Z. Zhu, Q. Wu, S. N. Gao, W. B. Hua, S. Indris, J. Chen, F. J. Li, *J. Am. Chem. Soc.*, 2023, **145**, 1564-1571.

88 M. H. Yang, Y. Wang, Y. F. Huang, J. M. Xiao, G. Y. Zhu, Y. Fang, X. C. Zhou, J. H. Long, M. Xie, D. S. Bin, D. Li, *Angew. Chem. Int. Ed.*, 2024, DOI: 10.1002/anie.202421008.

89 J. Yin, N. Li, M. Liu, Z. Li, X. Wang, M. Cheng, M. Zhong, W. Li, Y. Xu and X. H. Bu, *Adv. Funct. Mater.*, 2023, **33**, 2211950.

90 J. Yin, X. Lian, Z. Li, M. Cheng, M. Liu, J. Xu, W. Li, Y. Xu, N. Li and X. H. Bu, *Adv. Funct. Mater.*, 2024, **34**, 2403656.

91 K. Shi, X. Liu, J. Sang, M. Zhang, D. Han, J. Gong, *Chem. Eng. J*, 2024, **499**, 156021.

92 L. Sporrer, Q. Guo, X. Li, A. W. Lashkova, F. Reichmayr, S. Fu, H. I. Wang, M. Bonn, X. Li, P. A. L. Schmidt, M. Wang, Y. Lu, Y. Vaynzof, M. Yu, X. Feng, R. Dong, *Angew. Chem. Int. Ed.*, 2024, doi: 10.1002/anie.202418390.

93 J. Park, M. Lee, D. Feng, Z. Huang, A. C. Hinckley, A. Yakovenko, X. Zou, Y. Cui, Z. Bao**,** *J. Am. Chem. Soc.,* 2018, **140**, 10315-10323.

94 L. Wang, Y. Ni, X. Hou, L. Chen, F. Li, J. Chen, *Angew. Chem. Int. Ed.,* 2020, **59**, 22126-22131.

95 B. Wang, J. Li, M. Ye, Y. Zhang, Y. Tang, X. Hu, J. He, C. C. Li, *Adv. Funct. Mater.*, 2022, **32**, 2112072.

96 M. Qi, L. Cheng, H. Wang, F. Cui, Q. Yang, L. Chen, *Adv. Mater.*, 2024, **36**, 2401878.

97 D. Chen, L. Cheng, W. Chen, H. Wang, F. Cui, L. Chen, *Chem. Sci.*, 2024,**15**, 141564-11571.

98 G. Fang, J. Zhou**,** A. Pan, S. Liang, *ACS Energy Lett.*, 2018, **3**, 2480-2501.

99 K. W. Nam, S. S. Park, R. d. Reis, V. P. Dravid, H. Kim, C. A. Mirkin, J. F. Stoddart, *Nat. Commun.*, 2019, **10**, 4948.

100 Z. Sang, J. Liu, X. Zhang, L. Yin, F. Hou, J. Liang, *ACS Nano*, 2023, **17**, 3077-3087.

101 J. Liu, Y. Zhou, G. Xing, M. Qi, Z. Tang, O. Terasaki, L. Chen, *Adv. Funct. Mater.*, 2024, **34**, 2312636.

102 P. L. Bao, L. Q. Cheng, X. L. Yan, X. M. Nie, X. Su, H. G. Wang, L. Chen, *Angew. Chem. Int. Ed.*, 2024, **63**, e202405168.

103 L. Cheng, M. Qi, J. Yu, X. P. Zhang, H. G. Wang, F. Cui, Y. Wang**,** *Angew. Chem. Int. Ed.,* 2024, **63**, e202405239.

104 J. Wang, H. Jia, Z. Liu, J. Yu, L. Cheng, H. Wang, F. Cui, G. Zhu, *Adv. Mater.*, 2024, **36**, 2305605.

105 M. Yang, X. Zeng, M. Xie, Y. Wang, J. Xiao, R. Chen, Z. Yi, Y. Huang, D. Bin, D. Li, *J. Am. Chem. Soc.*, 2024, **146**, 6753-6762.

106 Y. Mu, J. Nyakuchena, Y. Wang, J. R. Wilkes, T. T. Luo, M. Goldstein, B. Eler, U. Mohanty, J. L. Bao, J. Huang, D. W. Wang, *Angew. Chem. Int. Ed.*, 2024, **63**, e202409286.

107 H. Y. Lu, J. S. Hu, K. Q. Zhang, Y. Zhang, B. T. Jiang, M. Zhang, S. Z. Deng, J. X. Zhao, H. Pang, B. G. Xu, *Adv. Mater.*, 2024, **36**, 2408396.

108 T. Guo, Y. C. Ding, C. Xu, W. X. Bai, S. C. Pan, M. L. Liu, M. Bi, J. W. Sun, X. P. Ouyang, X. Wang, Y. S. Fu, J. W. Zhu, *Adv. Sci.*, 2023, **10**, 2302518.

109 S. Yang, Y. Guo, P. Zhao, H. Jiang, H. Shen, Z. Chen, L. Jiang, X. Xue, Q. Zhang, H. Zhang, *ACS Catal.*, 2024, **14**, 449-462.

110 Y. Liu, M. Liu, S. Shang, W. Gao, X. Wang, J. Hong, C. Hua, Z. You, Y. Liu, J. Chen, *ACS Appl. Mater. Interfaces*, 2023, **15**, 16991-16998.

111 Y. Li, J. Lv, S. Li, L. Dai, B. Wang, P. Li, *J. Mater. Chem. A*, 2024, **12**, 24549-24555.

Chemical Science Accepted Manuscript

Data availability

No primary research results, software or code have been included and no new data were generated or analysed as part of this review.

Chemical Science Accepted Manuscript